Dynamically coupled fluid–body interactions in vorticity-based numerical simulations

Jeff D. Eldredge [*]

Mechanical and Aerospace Engineering, University of California, Los Angeles, CA 90095, USA

Abstract

A novel method is presented for robustly simulating coupled dynamics in fluid–body interactions with vorticity-based flow solvers. In this work, the fluid dynamics are simulated with a viscous vortex particle method. In the first substep of each time increment, the fluid convective and diffusive processes are treated, while a predictor is used to independently advance the body configuration. An iterative corrector is then used to simultaneously remove the spurious slip – via vorticity flux – and compute the end-of-step body configuration. Fluid inertial forces are isolated and combined with body inertial terms to ensure robust treatment of dynamics for bodies of arbitrary mass. The method is demonstrated for dynamics of articulated rigid bodies, including a falling cylinder, flow-induced vibration of a circular cylinder and free swimming of a three-link 'fish'. The error and momentum conservation properties of the method are explored. In the case of the vibrating cylinder, comparison with previous work demonstrates good agreement.
© 2008 Elsevier Inc. All rights reserved.

Keywords: Computational fluid dynamics; Numerical methods; Vortex methods; Viscous incompressible flow; Flow-structure interaction; Biological locomotion

1. Introduction

A large class of problems in nature and technology involves an inherently unsteady and coupled interaction between fluid and a flexible structure. An intriguing subset of this class is characterized by large-scale deformation of the structure in response to the external, inertial/elastic and fluid dynamic forces it experiences. Representative problems in this subset include locomotion of aquatic organisms and similarly inspired vehicles, the aerodynamics of flexible wings (e.g. in insects or microscale aerial vehicles), and cardiovascular flows. In many of these problems, the dynamics of both entities are inextricably bound, and both the nonlinear and viscous behavior of the fluid are essential – that is, the full unsteady Navier–Stokes equations must be solved simultaneously with the (possibly nonlinear) elasticity equations of the body.

---

[*] Tel.: +1 310 206 5094; fax: +1 310 206 4830.
E-mail address: eldredge@seas.ucla.edu

Indeed, these coupled problems have, for some time, provided motivation for the development of computational algorithms which address such fluid-structure interaction in a fundamental fashion. A significant source of progress in this context has been in the field of computational aeroelasticity [10], in which the overarching goal is to predict the response of an elastic wing to unsteady fluid loading. It has become common in such analyses to join independently-developed codes for resolving the fluid and structural dynamics. This approach is natural, since the solvers devoted to each component have been developed and refined over several years. Thus, the coupled method's overall stability is determined by the means of time synchronization and exchange of information at the interface. To avoid full regeneration of the fluid grid in response to the moving and deforming boundary, many researchers have made use of moving grid techniques, such as Arbitrary Lagrangian Eulerian (ALE) [7] and transfinite interpolation [13] methods.

In the most basic sense, the physical coupling between the fluid and body can be described schematically as in Fig. 1. The fluid and body evolution are joined by kinematic (velocity) and dynamic (force) constraints at their interface. It is important to note that there is no cause and effect in this relationship, but merely a condition that all interface constraints be consistently met at the end of each time increment. Thus, the sense of the arrows in the loop depicted in Fig. 1 is arbitrary, and can just as well be reversed. The computational methodology applied to such a problem must be respectful of this consistency condition in order to provide an accurate and stable solution. The present work will introduce a novel and high-fidelity approach for simulating these interactions based on the relationship between vorticity creation and the interaction forces at the fluid–body interface.

It is worth noting that, for problems in the inviscid limit (that is, when dissipation in the system is absent), it is possible to avoid consideration of the fluid–body interaction force altogether, and treat the fluid and body as a single extended system. The effect of the inertial force exerted by the fluid on an accelerating body can be expressed in terms of a time-varying added mass, leading to a single set of dynamical equations for the combined system. This approach has been successfully demonstrated in a recent study of inviscid locomotion by Kanso et al. [11]. Within this inviscid framework, it is also possible to introduce simple models for vorticity shedding, via a Kutta condition for example, and track the motions of the resulting vortex singularities.

In the problems of interest in the present study, the inertial and viscous processes are equally important, and viscous action at the fluid–body interface generates vorticity that is diffused into the adjacent fluid. Thus, energy is continuously exchanged with the fluid and eventually dissipated by viscous processes. For moderate to large Reynolds numbers (say, greater than 10), the vorticity-bearing fluid occupies only a small fraction of the region in which the velocity and pressure are nonzero. The present numerical methodology exploits, to the extent possible, the computational efficiency that is inherent to this behavior. The algorithm is an extension of the viscous vortex particle method (VVPM) [6,12,16], in which the Navier–Stokes equations are solved in a particle form by the convection and diffusion of blobs of vorticity. In the VVPM, spurious slip between the fluid and solid is identified with an equivalent vortex sheet, and then annihilated by diffusing this sheet to adjacent vortex particles. The interactions between vortex particles automatically account for the correct behavior of the velocity at infinity; thus, computational elements are needed only where vorticity is nonzero.

The algorithm presented here is wrapped around the VVPM, and in essence follows the sense of fluid–body coupling depicted in Fig. 1. However, the kinematic constraint of the no-slip condition is expressed in terms of
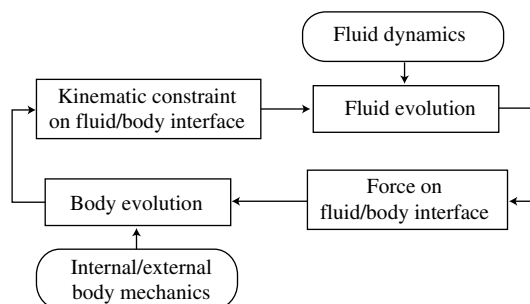

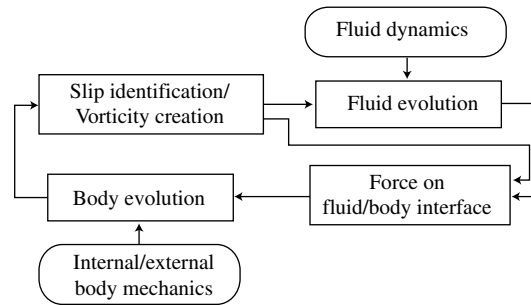Fig. 1. Schematic of coupling between fluid and body motion.

Fig. 2. Schematic of coupling in present algorithm.

vorticity creation, and the impulse associated with newly-fluxed vorticity contributes directly to the reaction force on the body; the viscous contribution to the force is expressed in terms of vorticity. This modified coupling is depicted in Fig. 2. In the first fractional step, the fluid is allowed to evolve independently (via convection and diffusion of the particles). To enable a consistent satisfaction of the kinematic and dynamic interface conditions at the end of the time step, a predictor–corrector scheme is used in which each corrector iteration for the new body configuration causes a trial vortex sheet to be fluxed to the particles. The resulting fluid force is used to update the body in the subsequent iteration. This procedure is carried out until convergence at each time step. To ensure robustness for any choice of body mass (including massless bodies), a virtual fluid inertia matrix is identified and added to the body inertia in the corrector equation. This approach extends a similar approach used by Shiels et al. [18] in their vortex method study of flow-induced vibration of massless bodies.

Though the resolution of the solid phase mechanics presents its own set of challenges, the focus of this work is on the solution in the fluid domain. Thus, in the examples presented in this work, the body mechanics are represented by a low-degree-of-freedom set of linked rigid bodies. However, the procedure that is described here holds equally well for more general body mechanics. The mathematical basis for the coupling methodology, as well as details of the implementation, are described in Section 2. Fluid dynamic forces and moments are expressed in a vorticity-explicit form in Section 2.1. The equations for the body dynamics, and in particular, their formulation for linked rigid bodies – which provide simple models for some biological systems – are described in Section 2.2. The algorithm of the method is illustrated in Section 2.4 for use in conjunction with the vortex particle method, and its use with other flow solvers is briefly discussed. In Section 3, the method is applied to illustrative problems involving two-dimensional rigid body motion. Numerical accuracy of the algorithm is evaluated on these example problems. Conclusions and future directions are discussed in Section 4.

2. Methodology

In this section, the algorithm and the details of its implementation will be described. The focus of this section is on the relationship between the body dynamics, the forces and moments exerted by the fluid, and the enforcement of interface conditions. Many of the details of the viscous vortex particle method (VVPM), which comprises the Navier–Stokes component of the interaction, will be omitted here; the reader is referred to previous work [3,6] for further information.

2.1. Fluid forces

The force and moment that a fluid exerts on a surface are generally expressed in terms of the integrated pressure and viscous stress. However, for incompressible flows, the viscous (resistive) component can easily be expressed in terms of vorticity, ω, and the pressure (reactive) contribution can be formulated in terms of vorticity flux, the buoyancy, and the displaced fluid inertia. The resulting expression for the force exerted by a fluid of density ρ_{f} and viscosity μ, in two-dimensional problems, is

$$\boldsymbol{F}^{\mathrm{f}} = \mu \oint_S \left[(\boldsymbol{x} - \boldsymbol{X}) \times \frac{\partial \boldsymbol{\omega}}{\partial n} - \boldsymbol{n} \times \boldsymbol{\omega} \right] \mathrm{d}s - \rho_{\mathrm{f}} A \boldsymbol{g} + \rho_{\mathrm{f}} A \dot{\boldsymbol{U}}, \tag{1}$$

where X is the body centroid position and ($\dot{\ }$) denotes differentiation with respect to time. Similarly, the moment about an axis passing through X_C (a point in arbitrary motion) is

$$
\mathbf{M}^{\mathrm{f}}|_C = \mu \oint_S (\mathbf{x} - \mathbf{X}_C) \times \left[\frac{1}{2} (\mathbf{x} - \mathbf{X}_C) \times \frac{\partial \boldsymbol{\omega}}{\partial n} - \mathbf{n} \times \boldsymbol{\omega} \right] \mathrm{d}s - 4\mu A \boldsymbol{\Omega} - (\mathbf{X} - \mathbf{X}_C) \times \rho_{\mathrm{f}} A \mathbf{g}
$$
$$
+ \rho_{\mathrm{f}} \left(2B + A|\mathbf{X} - \mathbf{X}_C|^2 \right) \dot{\boldsymbol{\Omega}} + (\mathbf{X} - \mathbf{X}_C) \times \rho_{\mathrm{f}} A \dot{\mathbf{U}}. \tag{2}
$$

The unit surface normal, $\mathbf{n}$, is directed into the fluid. The body is assumed to be rigid, and A denotes its area and B its second area moment of inertia. The linear and angular velocity of the body are represented by $\mathbf{U} = (U, V)$ and $\boldsymbol{\Omega} = \Omega \mathbf{e}_z$, respectively. In this paper, the vector and scalar representations of axial vectors such as angular velocity and the moment will be used interchangeably, for the sake of mathematical brevity.

The surface vorticity is calculated by differentiating the stream function field, $\omega = -\partial^2 \psi / \partial n^2$, with a 3rd-order-accurate formula at the wall [6]. The surface vorticity flux, $-v\partial\omega/\partial n$ (where $v = \mu/\rho_{\mathrm{f}}$), on the other hand, is computed by relying on the physical mechanism through which vorticity is created in the VVPM. In each timestep, the simultaneous evolution of the body and fluid leaves a spurious slip velocity, $\mathbf{u}_{\mathrm{slip}}$ (a non-vanishing velocity of the fluid relative to the local body velocity at the solid surface). The slip can be identified with a vortex sheet with strength distribution $\gamma = \mathbf{n} \times \mathbf{u}_{\mathrm{slip}}$, that must be instantly diffused into the surrounding fluid in order to satisfy the no-slip condition at the end of the timestep [14]. Using Kelvin's circulation theorem, the vorticity flux (the rate at which new vorticity is created) can be equated to the rate of disappearance of the spurious sheet over a time interval Δt, that is, $-v\partial\omega/\partial n = \gamma/\Delta t$. Subsequent to the diffusion of the sheet, the force and moment can be calculated with the corresponding terms in (1) and (2) replaced with this formula, leading to

$$
\mathbf{F}^{\mathrm{f}} = \mathbf{F}^{\gamma\omega} - \rho_{\mathrm{f}} A \mathbf{g} + \rho_{\mathrm{f}} A \dot{\mathbf{U}}, \tag{3}
$$

$$
\mathbf{M}^{\mathrm{f}}|_C = \mathbf{M}^{\gamma\omega}|_C - (\mathbf{X} - \mathbf{X}_C) \times \rho_{\mathrm{f}} A \mathbf{g} + \rho_{\mathrm{f}} (2B + A|\mathbf{X} - \mathbf{X}_C|^2) \dot{\boldsymbol{\Omega}} + (\mathbf{X} - \mathbf{X}_C) \times \rho_{\mathrm{f}} A \dot{\mathbf{U}}, \tag{4}
$$

in which, for later convenience, we have defined $\mathbf{F}^{\gamma\omega}$ and $\mathbf{M}^{\gamma\omega}|_C$ to represent the contributions of the viscous terms and the vortex sheet

$$
\mathbf{F}^{\gamma\omega} = -\rho_{\mathrm{f}} \oint_S \left[(\mathbf{x} - \mathbf{X}) \times \frac{\gamma}{\Delta t} + v\mathbf{n} \times \boldsymbol{\omega} \right] \mathrm{d}s, \tag{5}
$$

$$
\mathbf{M}^{\gamma\omega}|_C = -\rho_{\mathrm{f}} \oint_S (\mathbf{x} - \mathbf{X}_C) \times \left[\frac{1}{2} (\mathbf{x} - \mathbf{X}_C) \times \frac{\gamma}{\Delta t} + v\mathbf{n} \times \boldsymbol{\omega} \right] \mathrm{d}s - 4\mu A \boldsymbol{\Omega}. \tag{6}
$$

Expressions (3) and (4) are physically enlightening, particularly in the representation of the reaction force. When a body is accelerated from rest in a stagnant fluid, the impulse associated with the instantaneous appearance of a surface vortex sheet, in combination with the displaced fluid inertia, collectively account for the reaction of the fluid. In an inviscid problem, this reaction can be represented in terms of acceleration of a virtual mass of fluid. In a viscous problem, the vortex sheet is instantly diffused into the surrounding fluid, and thenceforth its effect is felt through its contribution to shear stress, as well as indirectly through the convection and diffusion of vorticity within the fluid.

Even in a viscous problem, terms that resemble the virtual inertia can be identified in expressions (3) and (4). Such an identification was made by Shiels et al. [18], who exploited it to investigate the flow-induced vibration of a cylinder when the intrinsic mass of the cylinder vanishes. The identification is made here in the same spirit, in anticipation of the time marching algorithm to be presented in Section 2.4. First, the terms proportional to $\mathrm{d}U/\mathrm{d}t$, $\mathrm{d}V/\mathrm{d}t$ and $\mathrm{d}\Omega/\mathrm{d}t$ are obvious contributors of fluid inertia. In addition, it is recalled that the vortex sheet strength on body j, $\gamma^{(j)}$, represents the spurious slip that results when the fluid vorticity and the bodies evolve independently in a given time step. As such, this strength can be linearly decomposed into a portion $\gamma_\omega^{(j)}$ due entirely to the vorticity-induced velocity when the bodies are instantaneously brought to rest in this step, and independent portions from each body's three velocity components in otherwise quiescent fluid (since motion of any single body will give rise to a vortex sheet on every body). This decomposition can be written as

$$\gamma^{(j)} = \gamma_\omega^{(j)} + \sum_{l=1}^{N_b} (\gamma_{U,l}^{(j)} U_l + \gamma_{V,l}^{(j)} V_l + \gamma_{\Omega,l}^{(j)} \Omega_l) \tag{7}$$

for a system with N_b bodies. This expression implies a similar decomposition in the fluid force and moment from the vortex sheet reactions in (5) and (6). For example, we can write the x component of $\boldsymbol{F}^{\gamma\omega}$ on body j as

$$F_{x,j}^{\gamma\omega} = -\rho_f \oint_{S_j} \left[(y - Y_j) \frac{\gamma_\omega^{(j)}}{\Delta t} + v n_y \omega \right] ds - \frac{1}{\Delta t} \sum_{l=1}^{N_b} (M_{Ux,lj}^* U_l + M_{Vx,lj}^* V_l + M_{\Omega x,lj}^* \Omega_l). \tag{8}$$

The first term represents the x component of the force on body j that would be felt if all bodies were brought to rest in interval Δt. The inertial role of the contributions from the unit vortex sheet components in (7) has been explicitly identified here, for example

$$M_{Ux,lj}^* = \rho_f \oint_{S_j} (y - Y_j) \gamma_{U,l}^{(j)} ds. \tag{9}$$

This coefficient (when divided by $-\Delta t$) approximately represents the x component of the reaction force felt on body j when body $l \neq j$ is accelerated from rest to unit velocity in the x direction. When $l = j$, the fluid inertia displaced by the body (from the final term in Eq. (3)) must be subtracted from the coefficient to give similar interpretation. Similar expressions can be found for $F_{y,j}^{\gamma\omega}$ and $M_j^{\gamma\omega}|_C$, giving rise to $9N_b^2$ such inertial coefficients. However, when constraints between linked bodies are accounted for, as they will be below, this total is reduced considerably.

2.2. Body dynamics

The objective of this section is to develop dynamical equations for two classes of problems of interest in this work: free swimming of a linked system and prescribed flapping of a multicomponent wing with passive elastic hinges. For the first class, the angles of the hinges are prescribed (to mimic, for example, the undulating backbone of an elongated fish), and the locomotion of the system must be solved for. In the second class, the motion of a certain reference point is prescribed (for example, by the attached musculature of an insect wing), and the hinge deflections must be solved for. Once the linkage constraints are accounted for, the state vector of the free swimming problem is reduced to the configuration and rate of change of a reference body in the system, and the input vector is the set of hinge angular velocities; in the flexible flapping problem, these roles are reversed.

Consider a set of N_b rigid bodies immersed in the fluid. Each body's configuration is described by the position of its centroid, $\boldsymbol{X}_j = (X_j, Y_j)$, in an inertial coordinate system, and its angle with respect to the positive x axis, α_j, which are written together as a configuration vector, $\mathcal{X}_j = (X_j, Y_j, \alpha_j)^T$. The rate of change of this configuration is determined by the body velocity, $\mathcal{U}_j = (U_j, V_j, \Omega_j)^T$. The uniform density of body j is denoted by ρ_j.

We suppose in this development that these bodies form a linked system (see Fig. 3), connected by $N_h = N_b - 1$ virtual hinges at $\boldsymbol{X}_j^h = (X_j^h, Y_j^h)$ that may be composed of passive torsion springs and dampers or actively manipulated 'motors' that control the angle of the hinge. The bodies are numbered sequentially from 1 to N_b, and the hinges between them from 1 to N_h. It is noted that the configuration of the system can be entirely described by $N_h + 3$ values: the configuration of a reference body (denoted by index k) and the N_h hinge angles. The development of dynamical equations for two classes of problems – free swimming of an articulated fish, and flapping of a multi-component wing – is described in detail in the Appendix. The equations are summarized here.

For free swimming, the system of linked bodies is subject only to the fluid dynamic forces and elastic/damping forces from springs attached to the reference body components; the hinge angles are prescribed functions of time. The dynamical equations are expressed in terms of the rates of change of position and velocity of reference body k

$$\dot{\mathcal{X}}_k = \mathcal{U}_k, \tag{10}$$

$$\mathbb{M}_k \dot{\mathcal{U}}_k = -\mathbb{M}_{\theta k} \ddot{\Theta} + \mathcal{F}_k^f + \mathcal{J}_k + \mathcal{G}_k - \mathbb{K}_k (\mathcal{X}_k - \mathcal{X}_{k0}) - \mathbb{R}_k \mathcal{U}_k, \tag{11}$$
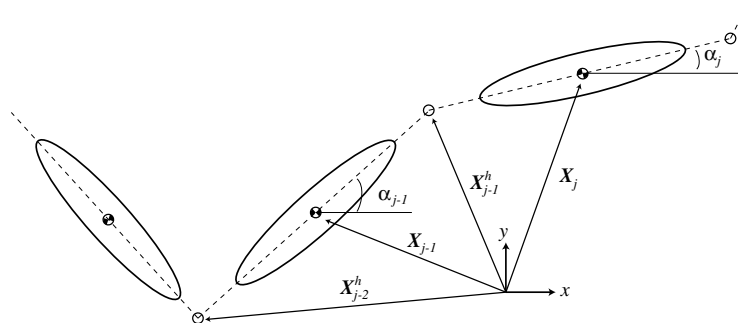
Fig. 3. Diagram of linked system of bodies.

where $\mathbb{M}_k$ and $\mathbb{M}_{\theta k}$ are 3×3 and $3 \times N_{\mathrm{h}}$ inertia matrices, respectively. The first term on the right-hand side of (11) represents the hinge forcing, and Θ is a column array of hinge angles. Furthermore, $\mathcal{F}_k^{\mathrm{f}}$ represents collective forces and moments exerted by the fluid; $\mathcal{J}_k$ contains centrifugal forces; $\mathcal{G}_k$ is the net gravity and buoyancy contribution; and $\mathbb{K}_k$ and $\mathbb{R}_k$ are diagonal matrices with spring stiffnesses and damping coefficients applied on the respective components of the reference body (about an equilibrium designated by $\mathcal{X}_{k0}$).

In a flexible multi-component wing, we are interested in solving for the hinge deflection angles in response to prescribed motion of the reference body. The resulting equations are

$$\mathbb{M}_{\theta}\ddot{\Theta} = -\mathbb{M}_{k\theta}\dot{\mathcal{U}}_k + \mathcal{F}_{\theta}^{\mathrm{f}} + \mathcal{J}_{\theta} + \mathcal{G}_{\theta} - \mathbb{K}_{\theta}(\Theta - \Theta_0) - \mathbb{R}_{\theta}\dot{\Theta}. \tag{12}$$

Most of the terms have interpretation analogous to the free-swimming problem. In addition, $\mathbb{K}_{\theta}$ and $\mathbb{R}_{\theta}$ are $N_{\mathrm{h}} \times N_{\mathrm{h}}$ diagonal matrices of spring stiffnesses and damping coefficients, respectively, about equilibrium hinge angles, Θ_0.

Note that it is also possible to 'mix' the problems, for example by designating individual hinges and reference body components as 'active' or 'passive'. Such a mix may be important for investigations of autorotation phenomena in flexible flapping or passive extraction of energy by a flexible swimmer.

2.3. Extraction of fluid inertial forces

The implicit time marching algorithm to be presented in this work is made significantly more robust – in terms of its iterative convergence in each time step – by identifying additional inertial terms in the fluid forces and combining them with the body inertial terms. This identification was made in Eq. (8) for individual bodies, and is extended here to linked systems. The extension is based on the observation that the linkage constraints allow the vortex sheet decomposition (7) to be written as

$$\gamma^{(j)} = \gamma_{\omega}^{(j)} + \gamma_U^{(j)}U_k + \gamma_V^{(j)}V_k + \gamma_{\Omega}^{(j)}\Omega_k + \sum_{l=1}^{N_{\mathrm{h}}} \gamma_{\theta,l}^{(j)}\dot{\theta}_l. \tag{13}$$

In turn, the original $9N_{\mathrm{b}}^2$ inertial coefficients arising from the reactions to the $3N_{\mathrm{b}}^2$ unit vortex sheets reduce to $3N_{\mathrm{b}}(3 + N_{\mathrm{h}})$ coefficients from reactions to the new set of $N_{\mathrm{b}}(3 + N_{\mathrm{h}})$ sheets.

We can thus write the overall fluid force array – either $\mathcal{F}_k^{\mathrm{f}}$ or $\mathcal{F}_{\theta}^{\mathrm{f}}$ in equation (11) or (12), respectively – in a general form

$$\mathcal{F}^{\mathrm{f}} = \mathcal{F}^{\omega} - \mathbb{M}^*\mathcal{U}_k/\Delta t - \mathbb{M}_{\theta}^*\dot{\Theta}/\Delta t - \mathbb{M}^{**}\dot{\mathcal{U}}_k - \mathbb{M}_{\theta}^{**}\ddot{\Theta} - \mathcal{J}^{\mathrm{f}}. \tag{14}$$

The component $\mathcal{F}^{\omega}$ in (14) represents the force and moment due to the viscous shear stress, as well as the reactions from $\gamma_{\omega}^{(j)}$ on each body – in other words, the force and moment that would arise after all bodies are brought to rest in the interval Δt. The $\mathbb{M}^*$ and $\mathbb{M}_{\theta}^*$ matrices derive from the reactions to the unit vortex sheets in (13), as manifested in coefficients such as (9). These reactions, once computed, are subsequently used in the force arrays in (A.28) or (A.37) to form the three columns of $\mathbb{M}^*$ and N_{h} columns of $\mathbb{M}_{\theta}^*$.

The $\mathbb{M}^{**}$ and $\mathbb{M}_\theta^{**}$ matrices arise from the terms proportional to acceleration in the fluid force (3) and moment (4) expressions. They are nearly identical in structure (with opposite sign) to the corresponding body inertia matrices, $\mathbb{M}$ and $\mathbb{M}_\theta$, except for additional contribution from the impulse of vorticity inside the bodies. For example, for free swimming problems, these inertial matrices are

$$\mathbb{M}_k^{**} = -\sum_j \rho_{\mathrm{f}} \begin{pmatrix} A_j & 0 & -A_j(Y_j - Y_k) \\ 0 & A_j & A_j(X_j - X_k) \\ -A_j(Y_j - Y_k) & A_j(X_j - X_k) & 2(B_j + A_j|\boldsymbol{X}_j - \boldsymbol{X}_k|^2) \end{pmatrix} \tag{15}$$

and

$$\mathbb{M}_\theta^{**} = -\begin{pmatrix} -\Sigma'\mathbb{M}_{\mathrm{f}}'\mathbb{H}_y(k) \\ \Sigma'\mathbb{M}_{\mathrm{f}}'\mathbb{H}_x(k) \\ \Sigma'\mathbb{M}_{\mathrm{f}}'(\mathbb{D}_x^{b'}\mathbb{H}_x(k) + \mathbb{D}_y^{b'}\mathbb{H}_y(k)) + \Sigma'[2\mathbb{I}_{\mathrm{f}}' + \mathbb{M}_{\mathrm{f}}'((\mathbb{D}_x^{b'})^2 + (\mathbb{D}_y^{b'})^2)]\mathbb{S}(k) \end{pmatrix}, \tag{16}$$

where $\mathbb{M}_{\mathrm{f}}'$ and $\mathbb{I}_{\mathrm{f}}'$ are $N_{\mathrm{h}} \times N_{\mathrm{h}}$ diagonal matrices containing, respectively, the mass and moment of inertia of the fluid displaced by all non-reference bodies. The remaining quantities are defined in the Appendix. The final term in Eq. (14), $\mathcal{J}^{\mathrm{f}}$, contains centrifugal-like forces, with the same form as the $\mathcal{J}$ terms in (A.28) or (A.36), though with $\mathbb{M}_{\mathrm{f}}'$ replacing $\mathbb{M}'$.

It is also useful to group the first three terms in (14) in a single term, $\mathcal{F}^{\gamma\omega}$ – analogous to the similarly-named terms in the force and moment expressions for a single body (3) and (4) – containing forces and moments from the complete surface vortex sheets (i.e. the vorticity flux impulse) and the viscous effects:

$$\mathcal{F}^{\gamma\omega} = \mathcal{F}^\omega - \mathbb{M}^*\mathcal{U}_k/\Delta t - \mathbb{M}_\theta^*\dot{\Theta}/\Delta t. \tag{17}$$

2.4. Algorithm description

The numerical algorithm utilized for advancing the system of fluid and bodies is described here. As in previous implementations of the viscous vortex particle method [12,6], a fractional step algorithm is used to split each time increment into two substeps devoted to fluid evolution (convection and diffusion of vorticity) and boundary condition enforcement (elimination of the spurious vortex sheet), respectively. The body dynamics are advanced with a second-order predictor–corrector method. The first substep of the fluid algorithm is carried out simultaneously with and independently from the predictor of the body dynamics. Because of the consistency condition between the fluid–body interaction force and the no-slip condition, the corrector of the body dynamics is performed simultaneously (that is, iteratively) with the flux of surface vorticity. Thus, at the end of a given time step, the new vorticity created is consistent with the final configuration of the bodies.

Note that, in the VVPM, the instantaneous state of the fluid is completely described by the positions and strengths of the N_{p} vortex particles, $\mathcal{P}(t) = \{(\boldsymbol{x}_{\mathrm{p}}(t), \Gamma_{\mathrm{p}}(t)), p = 1, N_{\mathrm{p}}\}$. This state is advanced by integrating the Navier–Stokes equations, which in the VVPM are described in a Lagrangian (particle-based) form. The details of these equations can be found in previous work [6]; here, they are represented symbolically as

$$\dot{\mathcal{P}} = \mathcal{N}(\mathcal{P}, \mathcal{B}, \boldsymbol{\Theta}). \tag{18}$$

The dependence of these equations on the body configurations (expressed through $\mathcal{B} = (\mathcal{X}, \mathcal{U})$, $\boldsymbol{\Theta}$ and their derivatives) arises solely through the influence of body rotation on the convection of particles, via the Biot–Savart integral. In the implementation of the VVPM in [6], the exchange of particle strengths to simulate viscous diffusion is carried out without explicit enforcement of a boundary condition on the body surfaces, and thus the diffusion step is unaffected by the body configuration.

The body evolution equations take alternative forms depending on the class of problem under study: (10) and (11) for free swimming or (12) for flexible flapping, or possibly a mix of the two. The time marching algorithm is demonstrated here for the free swimming equations, but the approach holds equally well for a flexible multi-component wing, with the roles of $\mathcal{U}_k$ and $\boldsymbol{\Theta}$ switched. For brevity, the subscript k is suppressed, and the equations are written with the help of (14) and (17) in the form

$$\dot{\mathcal{X}} = \mathcal{U}, \tag{19}$$

$$(\mathbb{M} + \mathbb{M}^{**})\dot{\mathcal{U}} = -(\mathbb{M}_\theta + \mathbb{M}_\theta^{**})\ddot{\Theta} + \mathcal{F}^{\gamma\omega} + \widetilde{\mathcal{G}}, \tag{20}$$

where $\widetilde{\mathcal{G}} = \mathcal{J} - \mathcal{J}^{\mathrm{f}} + \mathcal{G} - \mathbb{K}(\mathcal{X} - \mathcal{X}_0) - \mathbb{R}\mathcal{U}$.

The predictor–corrector scheme to be presented here for the body dynamics is designed to ensure robustness for any choice of body mass. We first multiply both sides of the dynamics Eq. (20) by the inverse of the body inertia matrix, $(\mathbb{M} + \mathbb{M}^{**})^{-1}$. It is important to note that there is no reason to assume that this matrix is in fact invertible; indeed, we allow for the possibility that the constituent bodies are *neutrally buoyant*, in which case this matrix becomes singular. We only make the inversion here for demonstrative purposes, and will never rely on such an inversion in the actual algorithm. Formally, the coupled set of six ordinary differential equations for the reference body configuration and velocity can be written as

$$\dot{\mathcal{B}} = \mathcal{D}(\mathcal{B}, \Theta, \mathcal{P}), \tag{21}$$

where the influence of the particle configuration arises through the fluid force $\mathcal{F}^{\gamma\omega}$ in (20). Note that the argument Θ denotes dependence on the prescribed hinge angles and all their time derivatives. A second-order-accurate predictor–corrector scheme is used to advance this equation from time t^n to the next step, $t^{n+1} = t^n + \Delta t$. The predictor is an explicit Euler step

$$\mathcal{B}_{(0)} = \mathcal{B}_n + \Delta t \dot{\mathcal{B}}_n. \tag{22}$$

The second-order-accurate corrector is designed to allow a full body/fluid inertia matrix to multiply the new velocity $\mathcal{U}_{n+1}$. To ensure this, an extra time level is used, and the algorithm is

$$\mathcal{B}_{n+1} = 2\mathcal{B}_n - \mathcal{B}_{n-1} + \Delta t(\dot{\mathcal{B}}_{n+1} - \dot{\mathcal{B}}_n). \tag{23}$$

The three position equations in this set are straightforward; we focus here on manipulating the three velocity equations. Each term in these velocity equations is multiplied by $\mathbb{M}_{n+1} + \mathbb{M}_{n+1}^{**}$:

$$(\mathbb{M}_{n+1} + \mathbb{M}_{n+1}^{**})\mathcal{U}_{n+1} = (\mathbb{M}_{n+1} + \mathbb{M}_{n+1}^{**})(2\mathcal{U}_n - \mathcal{U}_{n-1} - \Delta t \dot{\mathcal{U}}_n) + \Delta t(\mathbb{M}_{n+1} + \mathbb{M}_{n+1}^{**})\dot{\mathcal{U}}_{n+1}. \tag{24}$$

The last term can be replaced with the dynamics Eq. (20), and we make use of the force decomposition (17) to bring the virtual inertia matrix $\mathbb{M}_{n+1}^*$ to the left-hand side:

$$\overline{\mathbb{M}}_{n+1}\mathcal{U}_{n+1} = (\mathbb{M}_{n+1} + \mathbb{M}_{n+1}^{**})(2\mathcal{U}_n - \mathcal{U}_{n-1} - \Delta t \dot{\mathcal{U}}_n) + \Delta t(-\overline{\mathbb{M}}_{\theta,n+1}\ddot{\Theta}_{n+1} + \mathcal{F}_{n+1}^\omega + \widetilde{\mathcal{G}}_{n+1}), \tag{25}$$

where for convenience, we have defined the total body/fluid inertia matrix, $\overline{\mathbb{M}} = \mathbb{M} + \mathbb{M}^* + \mathbb{M}^{**}$, and a similar matrix, $\overline{\mathbb{M}}_\theta$, for the hinge inputs. This implicit corrector equation for $\mathcal{U}_{n+1}$, together with the position equation, can be solved iteratively with the form

$$\mathcal{X}_{(m+1)} = 2\mathcal{X}_n - \mathcal{X}_{n-1} + \Delta t(\mathcal{U}_{(m)} - \mathcal{U}_n), \tag{26}$$

$$\mathcal{U}_{(m+1)} = (I - \overline{\mathbb{M}}_{(m)}^{-1}\mathbb{M}_{(m)}^*)(2\mathcal{U}_n - \mathcal{U}_{n-1} - \Delta t \dot{\mathcal{U}}_n) + \Delta t \overline{\mathbb{M}}_{(m)}^{-1}(-\overline{\mathbb{M}}_{\theta,(m)}\ddot{\Theta}_{n+1} + \mathcal{F}_{(m)}^\omega + \widetilde{\mathcal{G}}_{(m)}), \tag{27}$$

where I is the 3×3 identity matrix.

Eqs. (26) and (27) represent the primary contribution of this work. Note that the steps leading to them are followed analogously, with the roles of $(\Theta, \dot{\Theta})$ and $(\mathcal{X}, \mathcal{U})$ switched, to develop an equivalent corrector for a flexible multi-component wing. The important feature of the equations is that the total inertia matrix, $\overline{\mathbb{M}}$, is non-singular for *any* body mass. The sum of matrices $\mathbb{M}^*$ and $\mathbb{M}^{**}$ is positive definite (together, they represent the virtual mass of the surrounding fluid when vorticity is absent). This feature is critical for robust simulation of bodies of any intrinsic mass. We iterate until the velocity error, defined by

$$\epsilon_{(m+1)} = \max |\mathcal{U}_{(m+1)} - \mathcal{U}_{(m)}|, \tag{28}$$

(where the maximum is taken over the three components) falls below a certain threshold. The threshold, which clearly determines how many iterations are necessary, is generally chosen to be $10^{-3}\Delta t$.

In lieu of a formal proof, we demonstrate the algorithm robustness on the example of a circular cylinder that is allowed to move freely in the y direction, transverse to a uniform free stream. Eq. (27) for the transverse velocity at time t^{n+1} reduces to

$$V_{(m+1)} = \frac{\rho_1}{\rho_1 + \rho_f}(2V_n - V_{n-1} - \Delta t \dot{V}_n) + \frac{\Delta t}{(\rho_1 + \rho_f)A_1}F_{y,(m)}^f + \frac{\rho_f}{\rho_1 + \rho_f}V_{(m)}, \tag{29}$$

where we have used Eq. (14) and a second-order extrapolation for the acceleration (consistent with (23)) to substitute the force F_y^ω with the full fluid force F_y^f. The velocity error is therefore governed by

$$\epsilon_{(m+1)} = \left| \frac{\rho_f}{\rho_1 + \rho_f} + \frac{\Delta t}{(\rho_1 + \rho_f)A_1} \frac{\partial F_y^f}{\partial V} \right| \epsilon_{(m)}. \tag{30}$$

For convergence, the factor on the right-hand side must be less than unity. The first term in the factor is, at most, unity, when the density of the cylinder vanishes. The second term is always negative, as the fluid force acts opposite the direction of cylinder motion. Thus, convergence is ensured for all choices of body mass.

The slowest convergence arises in problems involving massless bodies, for which four to six iterations are generally necessary; in neutrally buoyant or heavier bodies, only two or three are needed. We will demonstrate the convergence of this iterative form of the equation in the example problems of Section 3.

2.4.1. Initialization

At the start of a simulation, the fluid and bodies are presumed to be at rest. When the system input (either hinge angle actuation for free swimming, or reference point motion for a flexible wing) is instantly activated at $t = 0$, the velocity components in the companion state vector are automatically determined by consideration of conservation of momentum. First, it is noted that the impulsive reaction from the fluid is, through Eq. (17)

$$\int_{0-}^{0+} \mathcal{F}^{\gamma\omega}\,\mathrm{d}t = -\mathbb{M}^*\mathcal{U}(0^+) - \mathbb{M}_\theta^*\dot{\Theta}(0^+) \tag{31}$$

for either class of problem. Thus, upon integrating either dynamical Eq. (11) or (12) over this infinitely short interval, one arrives at a relation between the initial reference body velocity and the initial hinge angular velocities

$$(\mathbb{M} + \mathbb{M}^* + \mathbb{M}^{**})\mathcal{U}(0^+) + (\mathbb{M}_\theta + \mathbb{M}_\theta^* + \mathbb{M}_\theta^{**})\dot{\Theta}(0^+) = 0. \tag{32}$$

The initial velocities in the state vector (either $\mathcal{U}$ or $\dot{\Theta}$) are determined from this relation, and the remaining body velocities are determined through the linkage constraints. In turn, vortex sheets are identified with the resulting slip on the bodies, and each sheet is diffused into the fluid to form the initial vorticity field, $\mathcal{P}_0$.

2.4.2. Algorithm summary

The procedure for advancing the state of the bodies and fluid from t^n to $t^{n+1} = t^n + \Delta t$ is summarized here:

Substep 1: *Fluid evolution*
The particle state vector $\mathcal{P}_n$ is advanced to an intermediate value, $\tilde{\mathcal{P}}_{n+1}$, by integrating Eq. (18) with an explicit fourth-order Runge–Kutta scheme. However, in each Runge–Kutta stage, the body configurations are held at their initial values, $\mathcal{X}_n$ and $\mathcal{U}_n$.

Substep 1′: *Body predictor*
Simultaneously with substep 1, the predictor is computed

$$\mathcal{B}_{(0)} = \mathcal{B}_n + \Delta t \dot{\mathcal{B}}_n. \tag{33}$$

Substep 2: *Body evolution/vorticity creation*
The final fluid state, $\mathcal{P}_{n+1}$, is composed of the convected and diffused field from substep 1, plus a correction field, $\Delta\mathcal{P} = \{(0, \Delta\Gamma_p), p = 1, N_p\}$, which represents vorticity creation to enforce the no-slip condition. Thus, the solutions for $\Delta\mathcal{P}$ and $\mathcal{B}_{n+1}$ are solved simultaneously, via the corrector Eqs. (27) and (26), as follows:

    (2a) *Fluid correction field computed*
Based on the current body configuration, $\mathcal{B}_{(m)}$, the correction field $\Delta\mathcal{P}_{(m)}$ is computed in two parts to eliminate the spurious slip at the fluid–body interface. The usual treatment of the VVPM – to identify the strengths of the equivalent surface vortex sheets, and diffuse

these sheets to the adjacent vortex particles – is utilized here to eliminate this slip. This approach leads to sheets of strength $\gamma^{(j)}$, $j = 1, \ldots, N_b$, which, when diffused, collectively provide $\Delta \mathcal{P}_{(m)}$. Note that the solution for each $\gamma^{(j)}$ is carried out with a boundary element method, with the additional constraints imposed by Kelvin's circulation theorem

$$\oint_{S_j} \gamma^{(j)} \, \mathrm{d}s = -2A_j(\Omega_{(m),j} - \Omega_{n,j}) \tag{34}$$

for each body, and the correction strengths are explicitly forced to satisfy, $\sum_p \Delta \Gamma_{(m),p} = -2\sum_j A_j(\Omega_{(m),j} - \Omega_{n,j})$, to maintain conservation of global circulation. The reader is referred to [6] for details. Also, for purposes of computing the fluid inertia matrices $\mathbb{M}^*_{(m)}$ and $\mathbb{M}^*_{\theta,(m)}$, each component sheet in the decomposition (13) is computed separately.

(2b) *Corrector iteration*

The current body configuration, $\mathcal{B}_{(m)}$, the corrected vorticity field, $\tilde{\mathcal{P}}_{n+1} + \Delta \mathcal{P}_{(m)}$ and component vortex sheet strengths are used to compute the terms on the right-hand side of the velocity corrector (27). The corrector Eqs. (26 and 27) are then evaluated for $\mathcal{B}_{(m+1)}$. In the first time step, we set $\mathcal{B}_{-1} = \mathcal{B}_0 - \Delta t \dot{\mathcal{B}}_0$, and the evolution equations revert to first-order-accurate.

(2c) *Convergence check*

The convergence is checked via the velocity error defined in (28). If not yet converged, the correction vorticity field $\Delta \mathcal{P}_{(m)}$ is removed from the vortex particles and the algorithm returns to (2a). If converged, then compute one last correction field, $\Delta \mathcal{P}_{(m+1)}$ and set $\mathcal{B}_{n+1} = \mathcal{B}_{(m+1)}$ and $\mathcal{P}_{n+1} = \tilde{\mathcal{P}}_{n+1} + \Delta \mathcal{P}_{(m+1)}$, and stop.

Substep 3: *Final acceleration vector*

The end-of-step acceleration vector $\dot{\mathcal{U}}_{n+1}$ is computed from the second-order extrapolation formula

$$\dot{\mathcal{U}}_{n+1} = \frac{1}{\Delta t}(\mathcal{U}_{n+1} - 2\mathcal{U}_n + \mathcal{U}_{n-1}) + \dot{\mathcal{U}}_n \tag{35}$$

for free swimming. An analogous expression is used for computing $\ddot{\Theta}_{n+1}$ for flexible wing problems.

Numerical convergence of error in this algorithm will be demonstrated for individual example problems in Section 3.

It is appropriate to point out here how the two crucial elements of this algorithm – simultaneous enforcement of the no-slip condition and evolution of body dynamics, and reliance on virtual fluid inertia for iterative convergence robustness – might be used in conjunction with other flow solvers. The first element fits naturally with other vorticity-based flow solvers. For example, the algorithm presented here would be relatively unchanged for the vorticity–streamfunction algorithm introduced by Calhoun [1], in which jumps in vorticity and vorticity flux at the surface are utilized in an immersed interface method to enforce kinematic boundary conditions. The vortex-in-cell method developed by Cottet and Poncet [4] and the vorticity-based Cartesian grid algorithm of Russell and Wang [17] would also readily admit the treatment presented here. With some minor modifications, the approach could also be used in conjunction with primitive variable formulations, particularly those in immersed boundary methodologies, since their calculation of the force distribution to enforce the kinematic boundary conditions could be carried out simultaneously with the evolution of body configuration. Taira and Colonius [19] have recently presented an immersed-boundary fractional step algorithm that has particularly intriguing possibilities in this regard.

The iterative robustness through virtual inertia can also be extended to other flow solvers. Though the algorithm appears to rely on a force decomposition peculiar to vortex particle methods, it can be arrived at in an alternative fashion. One would start from Eq. (24) without the $\mathbb{M}^{**}_{n+1}$ factor, substitute the final term with the dynamics Eq. (11), and simply add $(\mathbb{M}^*_{n+1} + \mathbb{M}^{**}_{n+1})\mathcal{U}_{n+1}$ to each side of the equation (using the previous iteration level on the right side, and the next level on the left-hand side). A similar iterative scheme to (26 and 27)

results, but the fluid force and moment appear in their non-decomposed form, thus permitting the scheme's use with other fluid solvers. The calculation of $\mathbb{M}^*$, though, generally requires an auxiliary potential flow solver.

2.5. Momentum diagnostics

Global linear and angular momenta may serve as useful diagnostics for evaluating any coupled time-marching algorithm, particularly in cases in which the externally-applied forcing is known or absent. In vorticity-based methods, the global momentum components have simple expressions in terms of moments of vorticity [22]. For example, the linear components of body/fluid momentum are

$$(R_{M,x}, R_{M,y}) = \sum_j (\rho_j - \rho_\mathrm{f}) A_j (\boldsymbol{U}_j - \boldsymbol{g}t) + \rho_\mathrm{f} \boldsymbol{P}, \tag{36}$$

where $\boldsymbol{P}$ is the linear impulse of vorticity in the fluid and bodies:

$$\boldsymbol{P} = \int_{A_\mathrm{f}} \boldsymbol{x} \times \boldsymbol{\omega}\, \mathrm{d}\boldsymbol{x} + 2 \sum_j A_j \boldsymbol{X}_j \times \boldsymbol{\Omega}_j. \tag{37}$$

Similarly, the out-of-plane component of global angular momentum (about the centroid of the reference body k) is

$$R_{M,\mathrm{ang}} = \sum_j (\rho_j - \rho_\mathrm{f}) \{ A_j [(\boldsymbol{X}_j - \boldsymbol{X}_k) \times (\boldsymbol{U}_j - \boldsymbol{g}t)]_z + B_j \Omega_j \} - \frac{1}{2} \rho_\mathrm{f} \beta \Big|_k, \tag{38}$$

where $\beta|_k$ is the angular impulse of vorticity in the fluid and bodies, evaluated about $\boldsymbol{X}_k$:

$$\beta|_k = \int_{A_\mathrm{f}} |\boldsymbol{x} - \boldsymbol{X}_k|^2 \omega\, \mathrm{d}\boldsymbol{x} + 2 \sum_j (A_j |\boldsymbol{X}_j - \boldsymbol{X}_k|^2 + B_j) \Omega_j. \tag{39}$$

In deriving (39), it has been assumed that the global circulation

$$\Gamma = \int_{A_\mathrm{f}} \omega\, \mathrm{d}\boldsymbol{x} + 2 \sum_j A_j \Omega_j, \tag{40}$$

vanishes. By Kelvin's circulation theorem, this is true for any system started from rest; furthermore, the vorticity flux method used in this work guarantees discrete conservation, as well (for confirmation, the reader is referred to [6]). In fact, in the absence of external forcing – with the exception of gravity – a system initially at rest will maintain

$$R_{M,x} = 0, \quad R_{M,y} = 0, \quad R_{M,\mathrm{ang}} = 0. \tag{41}$$

However, in contrast to circulation, the discrete versions of these global momenta will generally have non-zero residual values, and these residuals serve as numerical diagnostics. It is also possible to define a 'momentum error'

$$\epsilon_\mathrm{mom}(T) = \left[\frac{1}{N+1} \sum_{n=0}^{N} \left(R_{M,x}^2(t^n) + R_{M,y}^2(t^n) \right) \right]^{1/2}, \tag{42}$$

where N is chosen such that $t^N = T$. In the next section, the coupled time-marching algorithm developed in Section 2.4 will be evaluated with the use of these momentum diagnostics.

In passing, it is noted that the expressions (36) and (38) for momenta have been specialized to rigid bodies, as the rest of this paper has, but can also be written for more general body deformation.

3. Results and discussion

In this section, the coupled fluid–body time marching algorithm presented in Section 2.4 is applied to three representative problems, the last of which is designed as an abstraction of biological locomotion mechanics. The first problem involves a circular cylinder falling under its own weight in a viscous fluid. The second problem, the flow-induced vibration of a circular cylinder, is used as a validation exercise and the results are compared with previous work. The second problem is the free swimming of an articulated three-link 'fish,' which

was previously studied in an inviscid medium by Kanso et al. [11]; here, the influence of viscosity is accounted for. An example of the method applied to a flexible multi-component wing has not been included here for brevity; however, such an application is the subject of a current effort by the author [20,21].

In all cases, the VVPM is applied in the same form used in previous work [6]. In particular, computational particles are initially arranged on a Cartesian grid with uniform spacing, and remeshed every four to six time steps to the same grid. Particle population growth is controlled by a threshold $\epsilon_{trim} = 2 \times 10^{-4}$ on a particle's circulation relative to the fluid viscosity.

3.1. Falling circular cylinder

Consider a circular cylinder of diameter $D = 1$ and density $\rho = 2\rho_f$, released from rest in a fluid of viscosity $v = 0.005$ and a gravity field of strength $g = 1$ in the negative y direction (that is, $g^{1/2}D^{3/2}/v = 200$). The coupled VVPM algorithm is applied with $\Delta t = 0.01$ and uniform inter-particle spacing $\Delta x = 0.01$; the surface of the cylinder is discretized with $N_p = 272$ panels (the VVPM is not sensitive to this choice, provided that the panel size is on the same order as Δx; see [6] for a discussion). No symmetry constraint was enforced in these simulations. The wakes are not truncated in any fashion, to avoid the additional error that such a technique would introduce. Consequently, simulations on a single workstation were limited to durations for which the computational particle population was below roughly 5×10^5.

The vorticity field produced by the falling cylinder is depicted at four instants in Fig. 4. It is noted that, though the instantaneous Reynolds number VD/v reaches 260 during the course of the simulation, the wake remains symmetric in the absence of explicitly-applied perturbation. As a consequence, the wake vortices are stretched considerably in the process. The time histories of the position, velocity and acceleration of the cylinder are depicted in Fig. 5(a)–(c). The initial reaction to acceleration is inviscid, associated with the impulse of the spurious vortex sheet that appears on the cylinder surface. It is easy to show that the initial acceleration of the body centroid is consequently given by

$$\dot{V} = \frac{\rho - \rho_f}{\rho + \rho_f} g, \tag{43}$$

which is consistent with the initial value of $-1/3$ observed in Fig. 5(c). The acceleration approaches zero, though never reaches it during the course of the simulation. This slow approach to terminal velocity is likely
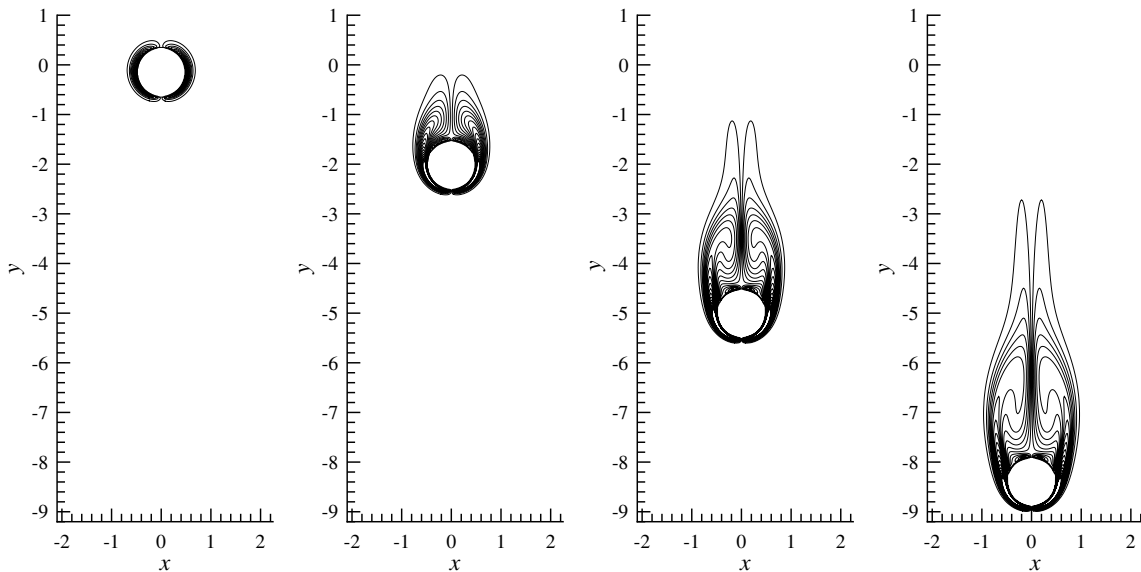

Fig. 4. Vorticity field generated by falling cylinder with $(gD^3)^{1/2}/v = 200$, shown at four instants, left to right: $(g/D)^{1/2}t = 1, 4, 7$ and 10. Vorticity contours have values from -10 to 10 in 40 uniform increments.
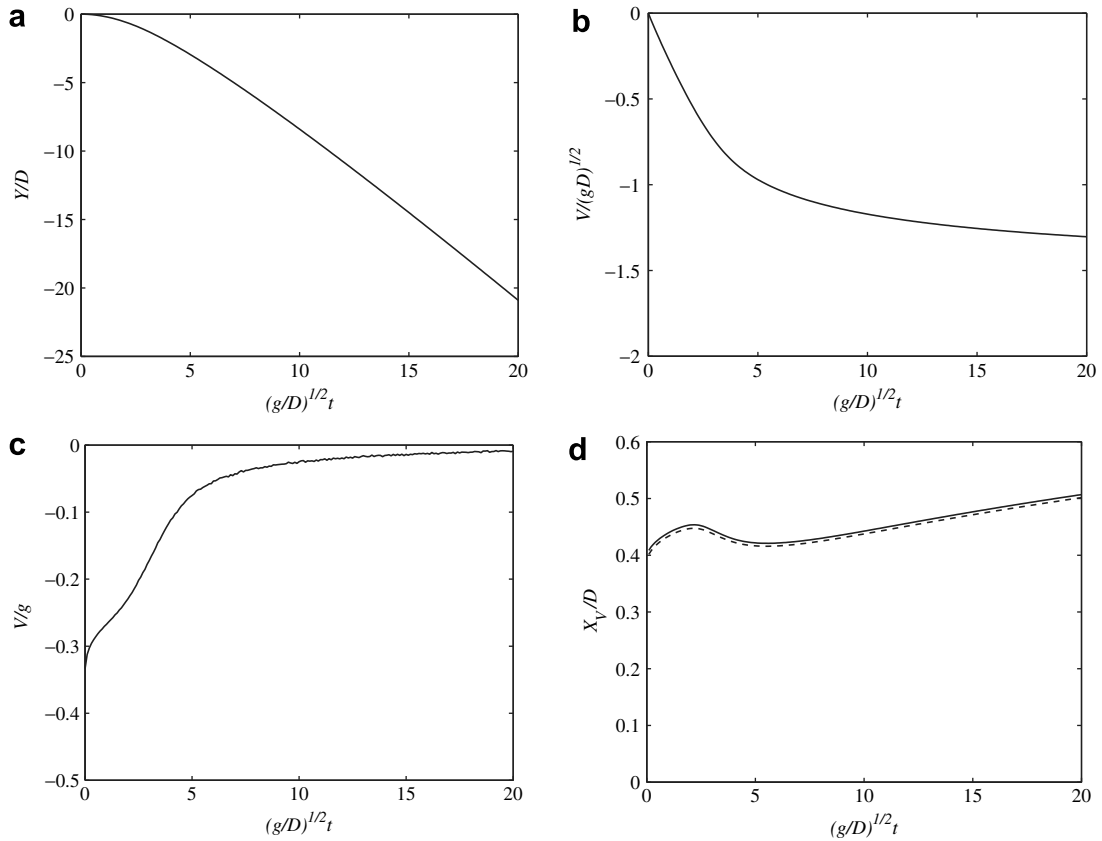
Fig. 5. (a) Position, (b) velocity and (c) acceleration of falling cylinder, computed with $\Delta t = 0.01$. (d) The time history of the x coordinate of the centroid of vorticity, with $\Delta t = 0.01$. Computed using $-P_y/(2\Gamma^+)$, —; and $(\rho - \rho_f)A(V + gt)/(2\Gamma^+)$, $---$.

attributable to lack of unsteady vortex shedding, which is generally present in free-falling experiments conducted at similar Reynolds numbers [9]. It is well known that, in this unstable regime, the drag coefficient of a circular cylinder is lower when the wake is symmetric and steady compared to its value at the same Reynolds number with unsteady vortex shedding [8]. Moreover, the drag decreases with Reynolds number on the steady branch, which would tend to increase the terminal velocity that is ultimately achieved.

The linear fluid impulse can be used to characterize the wake configuration. In particular, we define the x component of the vorticity centroid as $X_V = -P_y/(2\Gamma^+)$, where P_y is the y component of the impulse (37) and Γ^+ represents the total fluid circulation in the right-half plane

$$\Gamma^+ = \frac{1}{2} \int_{A_f} |\omega| \, d\mathbf{x}. \tag{44}$$

The evolution of this centroid coordinate is depicted in Fig. 5(d). The initial value of X_V can be predicted exactly from the impulse and circulation of the initial vortex sheet to be $\pi D/8$, in agreement with the simulation results. After an initial rise and recovery, the centroid increases very slowly at a nearly constant rate.

From the global momentum balance in Eq. (36), this centroid coordinate can be alternatively computed using $(\rho - \rho_f)A(V + gt)/(2\Gamma^+)$. The result from this alternative approach is also depicted in Fig. 5(d). A small error persists between the two approaches. This error is associated with the momentum residual, $R_{M,y}$, which is depicted in Fig. 6 after normalization by $(\rho - \rho_f)Agt$. The residual remains negative and less than 0.01 in magnitude throughout the simulation. It is important to check whether this momentum residual converges to zero as the resolution of the simulation is increased. In Table 1 the momentum error $\epsilon_{mom}(1)$ – normalized by the rms value of $(\rho - \rho_f)Agt$ up to $t = 1$ – is shown for four different values of time-step size, Δt. In each case, the
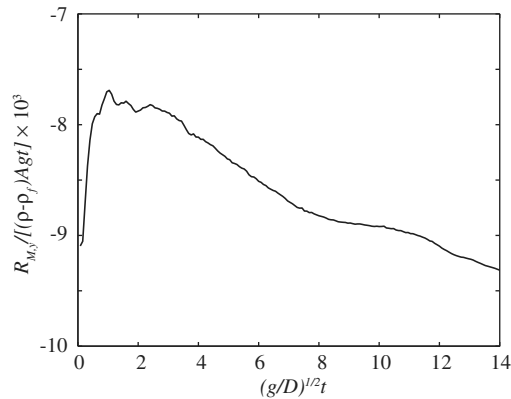
Fig. 6. Normalized residual of global conservation of vertical momentum, with $\Delta t = 0.01$.

Table 1
Momentum and differential trajectory errors for falling cylinder, evaluated up to $t = 1$

Δt	$\epsilon_{\mathrm{mom}}(1)$	$\epsilon_{\mathrm{traj}}(1)$
0.02	1.185×10^{-2}	3.429×10^{-4}
0.01	7.820×10^{-3}	8.798×10^{-5}
0.005	5.425×10^{-3}	1.896×10^{-5}
0.0025	3.945×10^{-3}	–

inter-particle spacing is adjusted so that the numerical parameter $\nu\Delta t/\Delta x^2$ is held fixed at 1/2. It is easy to see that this residual error indeed decreases as the resolution increases. However, the rate of convergence is slow, approximately $\Delta t^{0.5}$.

This slow convergence is attributable to particles nearest the body. The residuals contain error associated with the cumulative transfer of momentum between the fluid and bodies during the course of the simulation. However, it must also be noted that the calculation of the discrete versions of the vorticity impulses (37) and (39) also contributes error, as each particle carries a finite distribution of vorticity, which generally overlaps with the body in the body-adjacent particles. This overlap implies first-order accuracy in the surface treatment [6], which implies half-order convergence in time.

It is natural to ask whether this slow convergence affects other quantities in the fluid–body interaction. To assess this, we define a differential trajectory error, ϵ_{traj}, as

$$\epsilon_{\mathrm{traj}}(T) = \left[\frac{1}{N+1} \sum_{n=0}^{N} |Y_{\Delta t}^n - Y_{\Delta t/2}^{2n}|^2 \right]^{1/2}, \tag{45}$$

which measures the least-squares difference in trajectory between successive choices of resolution; the final time level, N, is chosen such that $N\Delta t = T$. This error is listed in the right-most column of Table 1 Richardson extrapolation can be used to estimate that the order of convergence of this trajectory is approximately 2, which is consistent with the second-order-accurate predictor–corrector scheme. Thus, the errors associated with the near-body treatment does not appear to affect the predicted trajectory.

3.2. Flow-induced vibration of a circular cylinder

A large number of experimental and numerical studies have been devoted to the transverse oscillations induced by unsteady vortex shedding from a circular cylinder. This problem is used here as a validation exercise, because the amplitude and frequency of oscillation, which are natural validation metrics, have been well characterized in the previous studies. Here, attention is focused on the case of a massless cylinder that is

allowed to move freely in the transverse direction with no damping or elastic constraints. This particular choice of parameters provides a demanding test of the coupling methodology, since the vibrations are completely determined by the exchanges between equal and opposite 'added-mass' and 'vortex wake' contributions to the transverse force. This case was explored by Shiels et al. [18] with a vortex particle method and coupling technique similar to the one used in the present work. In both this previous study and the present one, the Reynolds number is 100 and the flow is assumed to be two-dimensional.

The simulations are carried out with inter-particle spacing of 0.01, time-step size 0.01 and 300 panels on the body. The cylinder is allowed to passively move in the transverse (Y) direction, while its streamwise position is held fixed. To induce an unsteady wake and the accompanying free vibrations, the cylinder is rotated over the dimensionless time interval $t \in [0, 2]$ with angular velocity $\Omega = \sin \pi t$ and then prevented from rotating at all later times. In [18], beyond six cylinder diameters downstream the particles in the wake were merged into larger particles and viscous diffusion was turned off. This technique enabled longer simulation times and a more thorough exploration of the problem. In the present work, because attention is focused on the coupling algorithm and not the flow solver itself, no truncation or coarsening of the wake is carried out, and thus the simulation time is relatively restricted. Nevertheless, a meaningful comparison can be made with the results of Shiels at al. [18].

Fig. 7 depicts the time histories of the transverse position and the drag and lift coefficients. As Fig. 7(a) shows, the cylinder's motion quickly achieves a periodic and nearly sinusoidal vibration after approximately two oscillation cycles. Using a least-squares fit to a sinusoid over the final period, it was found that the amplitude of this vibration is approximately 0.45 and the frequency is 0.148. These values agree well with those reported by Shiels et al. [18], which were 0.47 and 0.156, respectively. The drag coefficient, shown in
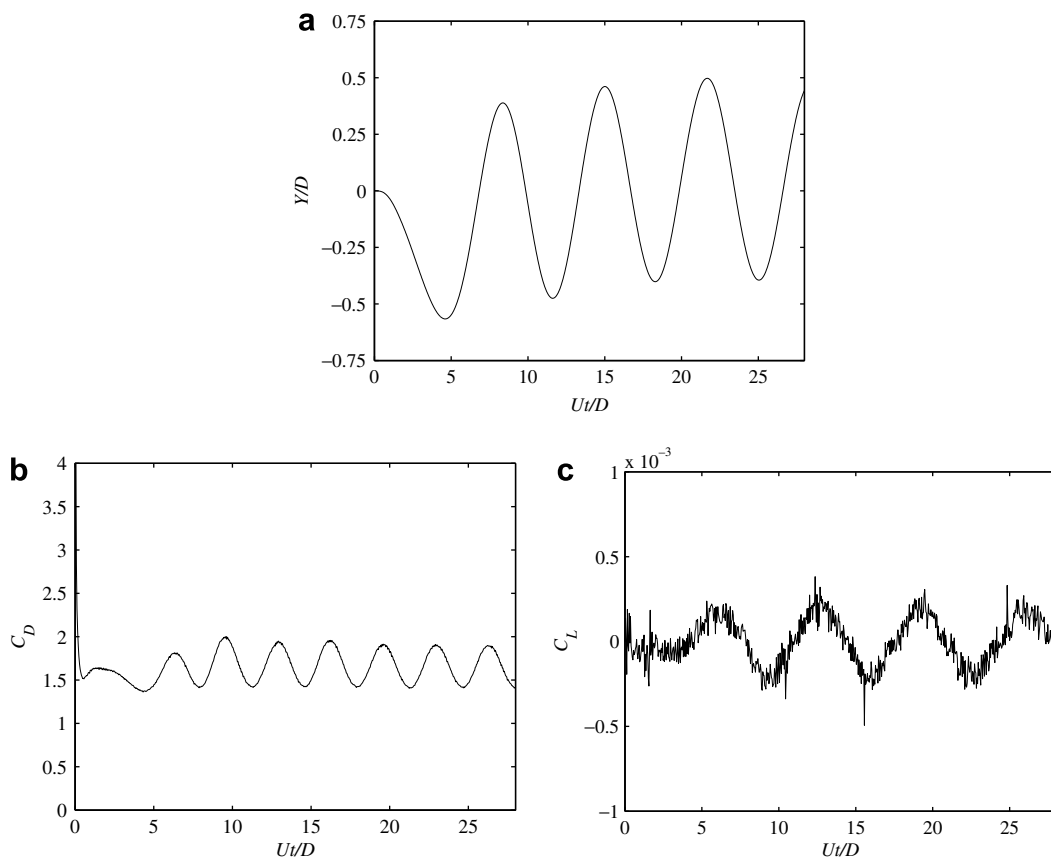

Fig. 7. Simulation of a freely vibrating cylinder in a free stream at $Re = 100$. (a) Transverse position. (b) Drag coefficient. (c) Lift coefficient.
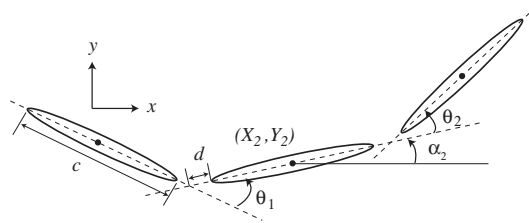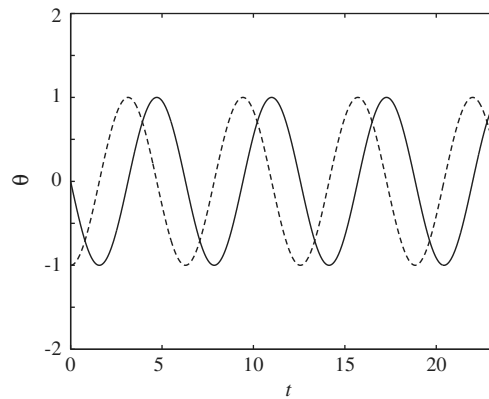
Fig. 8. Schematic of articulated three-body swimmer.

Fig. 9. Prescribed hinge angles of three-link swimmer: θ_1, —; θ_2, – – –.

Fig. 7(b), oscillates at twice the frequency of cylinder vibration, as expected from symmetry. The mean value over the final period of oscillation is 1.66, slightly smaller than the value of 1.73 reported in [18]. Finally, Fig. 7(c) depicts the lift coefficient over the course of the simulation. With no inertial or elastic forces acting on the cylinder, this lift should be zero. The magnitude of its computed value never exceeds 5×10^{-4}, and its mean is less than 2×10^{-6}.

### 3.3. Free swimming of an articulated fish

Undulatory locomotion is a persistent mechanism in aquatic lifeforms over an enormous range of Reynolds number (from spermatozoa to blue whales) [15]. The simplest representation of undulation in an elongated body consists of an articulated system of three linked rigid bodies (Fig. 8). Each of the two hinges is independently controlled, with its angle (θ_1 or θ_2) specified over all time. The resulting motion of the system is solved for, in this case in terms of the centroid position and angle of the central body (that is, $k = 2$).[1]

The self-propulsion of this system in an inviscid medium has recently been explored by Kanso et al. [11]. To coordinate the present simulations with these previous studies, three identical ellipses of aspect ratio 10 are used, and the distance from tip to hinge, d, is set to $0.1c$, where c is the length of each body. The prescribed hinge angles are

$$\theta_1(t) = -\cos(t - \pi/2), \quad \theta_2(t) = -\cos t, \tag{46}$$

---

[1] This problem was investigated in previous work by the author [5] using an earlier version of the present coupling algorithm; the results presented here are refinements of this former work. The earlier version used a lower-order corrector and an arbitrarily-chosen inertial term instead of the present extracted inertial force to ensure robustness for vanishing body inertia. The iterative scheme in the present work converges much more quickly.
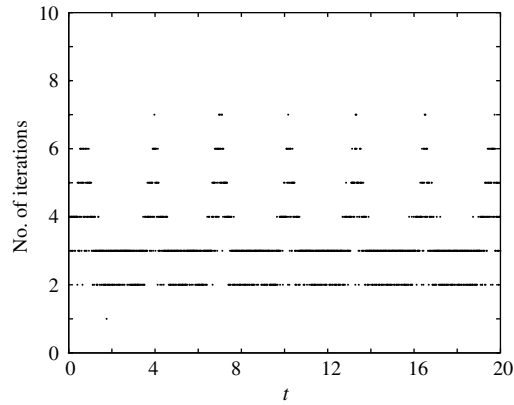
x
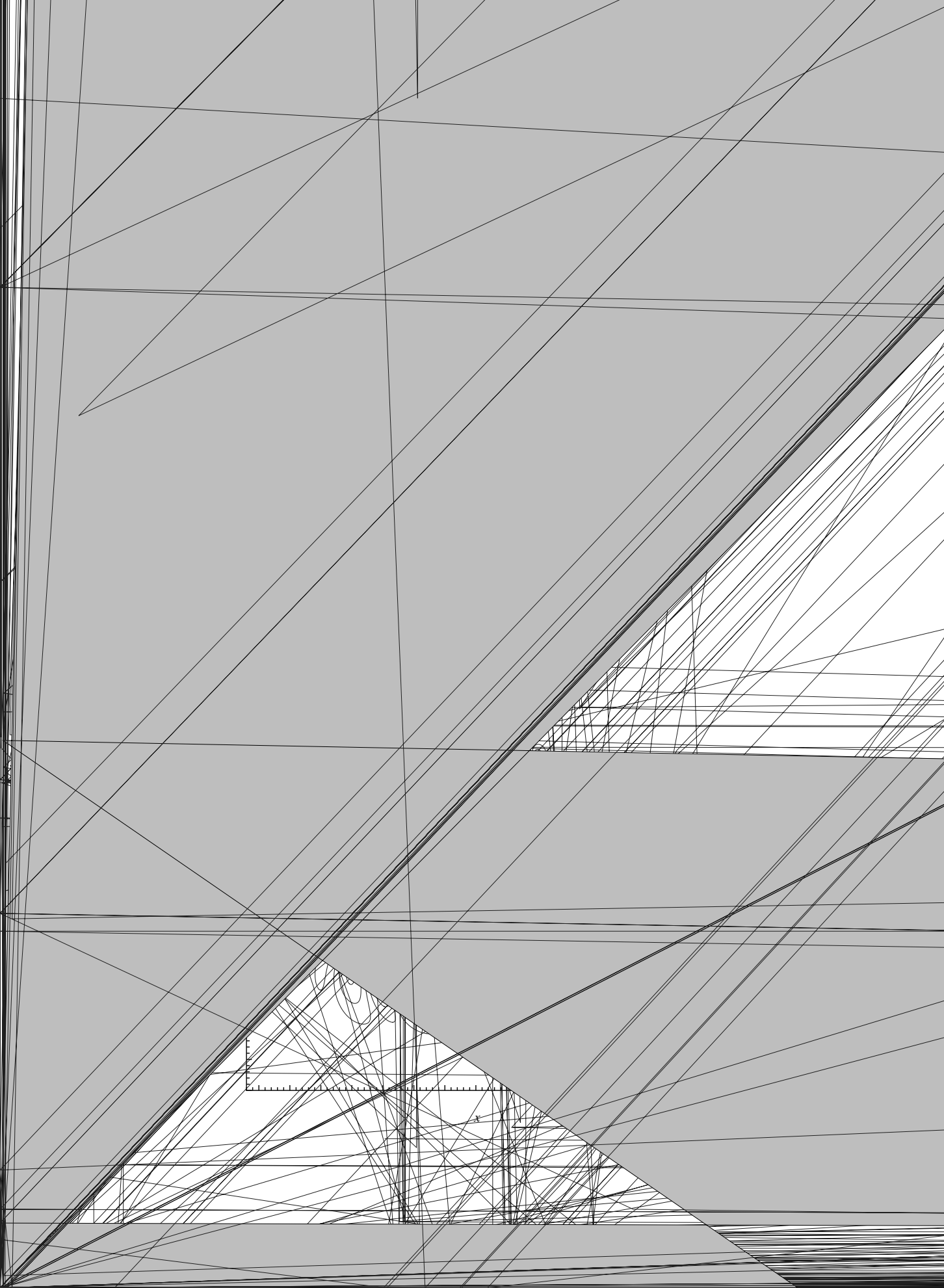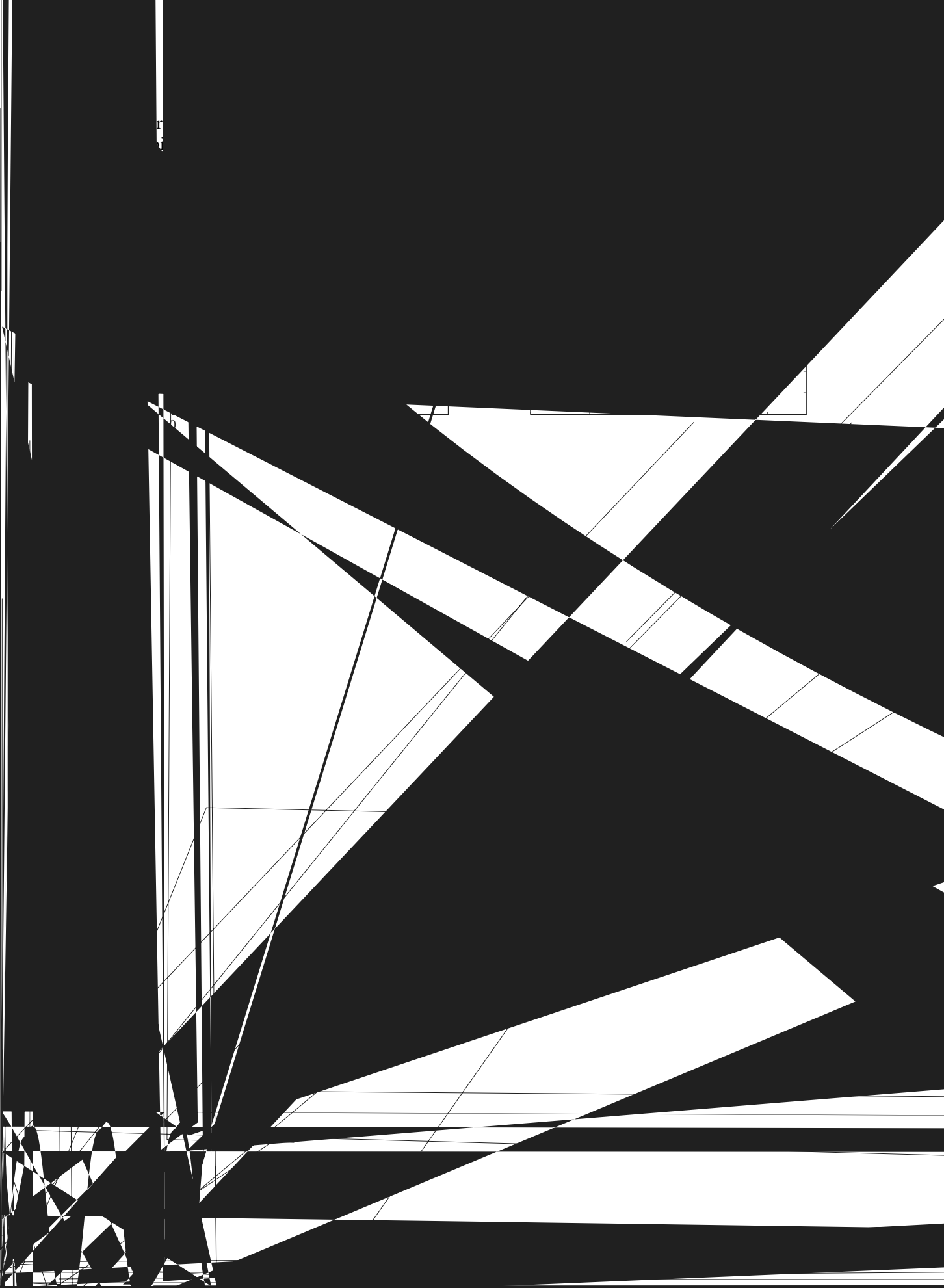
Fig. 13. Number of corrector iterations required to achieve threshold of 10^{-5} in massless three-link swimmer, with $\Delta t = 0.01$.
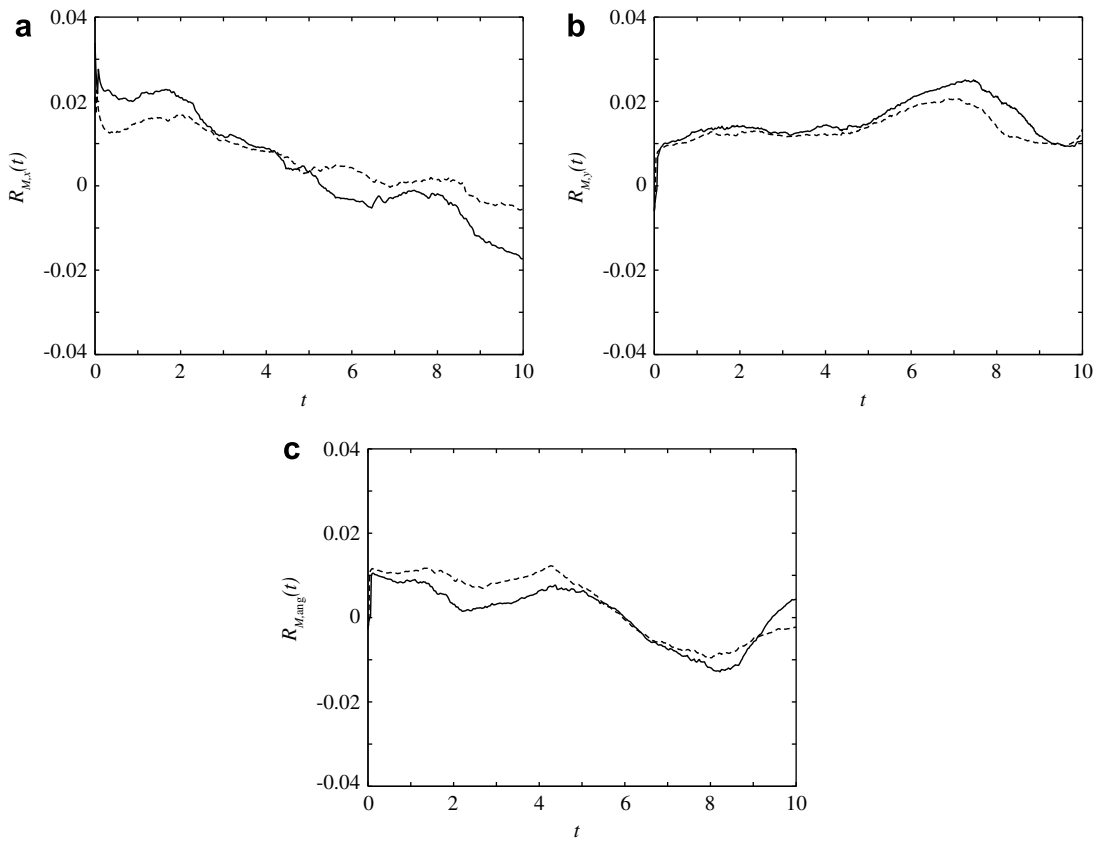
Fig. 14. Residual of global conservation of: (a) linear x-momentum, (b) linear y-momentum, and (c) angular momentum. Two different discretizations used: $\Delta t = 0.01$, —; $\Delta t = 0.005$, – – –.

Table 2
Momentum and differential trajectory errors for three-link swimmer, evaluated up to $t = 2$

Δt	$\epsilon_{mom}(2)$	$\epsilon_{traj}(2)$
0.02	4.103×10^{-2}	4.553×10^{-2}
0.01	2.382×10^{-2}	8.598×10^{-3}
0.005	1.846×10^{-2}	3.619×10^{-3}
0.0025	4.170×10^{-3}	–

are plotted in Fig. 11. It is clear that, after a brief start-up phase, the motion achieves nearly periodic behavior after one cycle. The rms velocity of this centroid is 0.238 and its peak speed is 0.373; the centroid travels approximately 0.72 chord-lengths (0.21 body-lengths) per period, at an angle of approximately 15° below the positive x axis.

The forces and moments exerted by the fluid on each constituent body are shown in Fig. 12; the moments are evaluated about the centroid of the central body. In each case, the force (or moment) is decomposed into contributions from the pressure and viscous shear stress. It should be noted that the total force and moment acting on the system (that is, the sum of pressure plus viscous parts across each row of the array of plots) must vanish at any instant, as no external forces or torques act on the system and the bodies have no inertia.

To illustrate the convergence of the iterative corrector scheme, the number of required iterations to reach the threshold of $10^{-3}\Delta t = 10^{-5}$ is shown in Fig. 13. This number varies with half the period of the underlying undulation, and reaches its largest value at approximately the times $\pi/4$, $5\pi/4$, $9\pi/4$, etc. It is noted that the envelope is similar in shape to $-|\dot{\theta}_1 + \dot{\theta}_2|/2$, suggesting that the slowest convergence coincides with minima in the average angular velocity of the hinges.

As in the previous example, the residual momenta serve as diagnostics for this free swimming problem. The histories of the three residual components are depicted in Fig. 14, for two different choices of time-step size, $\Delta t = 0.01$ and $\Delta t = 0.005$ (once again, $\nu\Delta t/\Delta x^2$ is fixed at 1/2). No trends are easily discernible due to the complex interactions in the transfer of momentum, as discussed in the previous problem. The momentum error (42), computed through $t = 2$, is tabulated in Table 2. The error is smaller for each successive decrease in Δt, though the rate of convergence is not constant.

The differential trajectory error, ϵ_{traj}, defined analogously to Eq. (45) in the previous example, is also shown in Table 2 (computed through $t = 2$). As in the previous example, this error decays more rapidly than the momentum error.

4. Conclusions

In this work, a novel method has been presented for robustly simulating coupled fluid–body interactions with vorticity-based solvers. The implicit time-marching method is made stable by respecting the consistency required between vorticity creation and the fluid reaction force. Fluid inertial forces have been isolated and combined with body inertial terms to ensure robust treatment of dynamics for bodies of arbitrary mass. The utility of the method has been demonstrated on three example problems, one of which is an abstracted model of biological mechanics of propulsion in fluids. The error and momentum conservation properties have been explored. It was found that the momentum residual converges slower than first order with respect to time-step size, due to error in the impulse associated with newly-created vorticity. However, this error has little effect on the computed trajectory of the bodies, which exhibits convergence at a rate consistent with the 2nd-order predictor–corrector scheme. An evaluation of the method on flow-induced vibration of a circular cylinder demonstrated good agreement with a previous numerical study.

Though the focus of this paper has been on the viscous vortex particle method, the approach is also applicable for other methods, such as vortex-in-cell [2,4] or vorticity-based Cartesian grid methods [1,17]. Furthermore, the time-marching method can be generalized to both continuously deforming bodies and three-dimensional flows, though some simplification is necessary to extend the fluid inertia extraction approach to deformable bodies. These extensions – as well as identification of means for computational acceleration – are the subjects of continuing work. In addition, the validation of the method – through comparison with physical experiments of the flexible flapping – is currently underway [20,21].

Finally, it is noted that the method can readily solve inviscid problems by simply suppressing the flux of the vortex sheet in each time step. The fluid is then in potential flow, which is entirely described by the boundary elements; furthermore, the force and moment are then entirely reactive. This provides the coupled tool with a distinct advantage over grid-based methods, whose inherent numerical dissipation makes such inviscid simulations challenging.

Acknowledgement

Appendix A. Development of articulated body dynamics equations

This appendix describes the development of dynamical equations for articulated bodies in two classes of problems of interest in this work: free swimming and flexible flapping. The basis for both is Newton's second law of motion and the constraints between inextensible linkages.

For body j with density ρ_j, the linear momentum is governed by

$$\rho_j A_j \dot{\boldsymbol{U}}_j = \rho_j A_j \boldsymbol{g} + \boldsymbol{F}_j^{\mathrm{f}} + \boldsymbol{F}_{j-1}^{\mathrm{h}} - \boldsymbol{F}_j^{\mathrm{h}}, \tag{A.1}$$

where the forces $\boldsymbol{F}_{j-1}^{\mathrm{h}}$ and $\boldsymbol{F}_j^{\mathrm{h}}$ are exerted by the two adjacent hinges. By convention, we define the force at the second hinge to be negative to explicitly represent it as the reaction from the adjacent body. The bodies are numbered sequentially from 1 to N_{b}, and the hinges between them from 1 to N_{h}; note that $\boldsymbol{F}_0^{\mathrm{h}}$ and $\boldsymbol{F}_{N_{\mathrm{b}}}^{\mathrm{h}}$ are both zero. The angular momentum of body j is governed by

$$(\boldsymbol{X}_j - \boldsymbol{X}_C) \times \rho_j A_j \dot{\boldsymbol{U}}_j + \rho_j B_j \dot{\boldsymbol{\Omega}}_j = (\boldsymbol{X}_j - \boldsymbol{X}_C) \times \rho_j A_j \boldsymbol{g} + \boldsymbol{M}_j^{\mathrm{f}}|_C + \boldsymbol{M}_{j-1}^{\mathrm{h}} + (\boldsymbol{X}_{j-1}^{\mathrm{h}} - \boldsymbol{X}_C) \times \boldsymbol{F}_{j-1}^{\mathrm{h}} - \boldsymbol{M}_j^{\mathrm{h}}$$
$$- (\boldsymbol{X}_j^{\mathrm{h}} - \boldsymbol{X}_C) \times \boldsymbol{F}_j^{\mathrm{h}}, \tag{A.2}$$

where $\boldsymbol{M}_{j-1}^{\mathrm{h}}$ and $\boldsymbol{M}_j^{\mathrm{h}}$ denote the moments exerted by the adjacent hinges (and $\boldsymbol{M}_0^{\mathrm{h}}$ and $\boldsymbol{M}_{N_{\mathrm{b}}}^{\mathrm{h}}$ are both zero). For an isolated body, the reference point $\boldsymbol{X}_C$ is conveniently chosen to be the centroid of the body; for a linked system, the reference is typically the centroid of some body in the system, denoted by index k, so that $\boldsymbol{X}_C = \boldsymbol{X}_k$.

Eqs. (A.1) and (A.2) can be written more compactly in matrix form as

$$\mathbb{M}\dot{\mathcal{U}} = \mathcal{F}_x^{\mathrm{f}} + \Delta\mathcal{F}_x^{\mathrm{h}} + (\mathbb{M} - \mathbb{M}_{\mathrm{f}})\mathcal{G}_x, \tag{A.3}$$

$$\mathbb{M}\dot{\mathcal{V}} = \mathcal{F}_y^{\mathrm{f}} + \Delta\mathcal{F}_y^{\mathrm{h}} + (\mathbb{M} - \mathbb{M}_{\mathrm{f}})\mathcal{G}_y, \tag{A.4}$$

$$-\mathbb{D}_y^{\mathrm{b}}\mathbb{M}\dot{\mathcal{U}} + \mathbb{D}_x^{\mathrm{b}}\mathbb{M}\dot{\mathcal{V}} + \mathbb{I}\dot{\Omega} = \mathcal{M}^{\mathrm{f}} - \mathbb{D}_y^{\mathrm{b}}\mathcal{F}_x^{\mathrm{f}} + \mathbb{D}_x^{\mathrm{b}}\mathcal{F}_y^{\mathrm{f}} + \Delta(\mathcal{M}^{\mathrm{h}} + \mathbb{D}_x^{\mathrm{h}}\mathcal{F}_y^{\mathrm{h}} - \mathbb{D}_y^{\mathrm{h}}\mathcal{F}_x^{\mathrm{h}}) + (\mathbb{M} - \mathbb{M}_{\mathrm{f}})(-\mathbb{D}_y^{\mathrm{b}}\mathcal{G}_x + \mathbb{D}_x^{\mathrm{b}}\mathcal{G}_y), \tag{A.5}$$

where $\mathcal{U}$, $\mathcal{V}$ and Ω are column vectors with the body velocity components; $\mathbb{M}$ and $\mathbb{I}$ are diagonal matrices with the body masses and moments of inertia, respectively; $\mathbb{M}_{\mathrm{f}}$ is a diagonal matrix with displaced fluid mass, and $\mathcal{G}_x$ and $\mathcal{G}_y$ are length-N_{b} column vectors with the gravity components in the respective directions; $\mathcal{F}_x^{\mathrm{f}}$, $\mathcal{F}_y^{\mathrm{f}}$ and $\mathcal{M}^{\mathrm{f}}$ are column vectors with the fluid dynamic force components in the x and y directions and the fluid moments about the corresponding body centroids, respectively; and $\mathcal{F}_x^{\mathrm{h}}$, $\mathcal{F}_y^{\mathrm{h}}$, and $\mathcal{M}^{\mathrm{h}}$ are column vectors with the hinge force components and moments, respectively. The matrix operators $\mathbb{D}_x^{\mathrm{b}}$ and $\mathbb{D}_y^{\mathrm{b}}$ are $N_{\mathrm{b}} \times N_{\mathrm{b}}$ diagonal with entries $X_j - X_k$ and $Y_j - Y_k$, respectively. Similarly, $\mathbb{D}_x^{\mathrm{h}}$ and $\mathbb{D}_y^{\mathrm{h}}$ are $N_{\mathrm{h}} \times N_{\mathrm{h}}$ diagonal with $X_j^{\mathrm{h}} - X_k$ and $Y_j^{\mathrm{h}} - Y_k$.

Two useful matrix operator for manipulating the dynamics equations are the $N_{\mathrm{b}} \times N_{\mathrm{h}}$ differencing operator Δ and a $j \times j$ lower triangular progressive sum Σ_j

$$\Delta = \begin{pmatrix} -1 & 0 & 0 & \cdots & 0 & 0 \\ 1 & -1 & 0 & \cdots & 0 & 0 \\ 0 & 1 & -1 & \cdots & 0 & 0 \\ \vdots & \vdots & \vdots & & \vdots & \vdots \\ 0 & 0 & 0 & \cdots & 1 & -1 \\ 0 & 0 & 0 & \cdots & 0 & 1 \end{pmatrix}, \qquad \Sigma_j = \begin{pmatrix} 1 & 0 & \cdots & 0 & 0 \\ 1 & 1 & \cdots & 0 & 0 \\ \vdots & \vdots & & \vdots & \vdots \\ 1 & 1 & \cdots & 1 & 0 \\ 1 & 1 & \cdots & 1 & 1 \end{pmatrix}. \tag{A.6}$$

The differencing operator has a companion family of progressive summation operators, $\mathbb{S}(k)$, defined as the following $N_{\mathrm{h}} \times N_{\mathrm{h}}$ matrix:

$$\mathbb{S}(k) = \begin{pmatrix} -\Sigma_{k-1}^{\mathrm{T}} & 0 \\ 0 & \Sigma_{N_{\mathrm{b}}-k} \end{pmatrix}, \tag{A.7}$$

where Σ_j^{T} denotes the upper triangular transpose of Σ_j. The argument of $\mathbb{S}$ can vary between 1 and N_{b}; for $k = 1$, the operator is purely lower triangular, $\Sigma_{N_{\mathrm{h}}}$, and for $k = N_{\mathrm{b}}$, the operator is upper triangular, $-\Sigma_{N_{\mathrm{h}}}^{\mathrm{T}}$.

Note that $\mathbb{S}(k)$ sums over all hinges that lie between a given body (expressed by the row number, with a jump past k) and the reference body k; for bodies that are below (have lower index than) the reference, the summation is negative. It is useful to note the following results. First, denote $\widetilde{\mathbb{S}}(k)$ as the matrix $\mathbb{S}(k)$, padded with an extra row of zeroes in the kth row. Then, for any $k = 1, \ldots, N_{\mathrm{b}}$

$$\Delta^{\mathrm{T}} \widetilde{\mathbb{S}}(k) = I_{N_{\mathrm{h}}}, \tag{A.8}$$

where $I_{N_{\mathrm{h}}}$ is the identity matrix of size $N_{\mathrm{h}} \times N_{\mathrm{h}}$. Furthermore

$$\widetilde{\mathbb{S}}(k)\Delta^{\mathrm{T}} = I_{N_{\mathrm{b}}} - \begin{pmatrix} 0 & 0 & \cdots & 1 & \cdots & 0 & 0 \\ 0 & 0 & \cdots & 1 & \cdots & 0 & 0 \\ \vdots & \vdots & & \vdots & & \vdots & \vdots \\ 0 & 0 & \cdots & 1 & \cdots & 0 & 0 \end{pmatrix}, \tag{A.9}$$

where the final matrix on the right-hand side is square of size N_{b}, and zero aside from a single column of ones in the kth column. For future use, it is noted that the hinge forces can be solved for from the linear momentum Eqs. (A.3),(A.4) by employing relation (A.8) in transposed form:

$$\mathcal{F}_x^{\mathrm{h}} = \widetilde{\mathbb{S}}^{\mathrm{T}}(k)(\mathbb{M}\dot{\mathcal{U}} - \mathcal{F}_x^{\mathrm{f}} - (\mathbb{M} - \mathbb{M}_{\mathrm{f}})\mathcal{G}_x), \tag{A.10}$$

$$\mathcal{F}_y^{\mathrm{h}} = \widetilde{\mathbb{S}}^{\mathrm{T}}(k)(\mathbb{M}\dot{\mathcal{V}} - \mathcal{F}_y^{\mathrm{f}} - (\mathbb{M} - \mathbb{M}_{\mathrm{f}})\mathcal{G}_y). \tag{A.11}$$

A.1. Linkage constraints

For isolated bodies, the hinge forces and moments are zero, and Eqs. (A.3),(A.5) – with associated position evolution equations – constitute a closed system. When the bodies are linked, however, these dynamical equations are supplemented by the constraints imposed by the hinges, which relate the centroid positions and velocities to those of the reference body and the angles of the hinges, θ_j, $j = 1, \ldots, N_{\mathrm{h}}$. For a given hinge, X_j^{h}, we label the lengths from the hinge to the two adjacent body centroids, X_j and X_{j+1}, as $L_{j,1}$ and $L_{j,2}$, respectively. Then, the centroids, hinge positions and body angles are related by the recurrence relations

$$X_j^{\mathrm{h}} = X_j + L_{j,1}\cos\alpha_j, \quad X_{j+1} = X_j^{\mathrm{h}} + L_{j,2}\cos\alpha_{j+1}, \tag{A.12}$$

$$Y_j^{\mathrm{h}} = Y_j + L_{j,1}\sin\alpha_j, \quad Y_{j+1} = Y_j^{\mathrm{h}} + L_{j,2}\sin\alpha_{j+1}, \tag{A.13}$$

$$\alpha_{j+1} = \alpha_j + \theta_j. \tag{A.14}$$

Differentiating these expressions, the centroid velocities of two adjacent bodies can be related by

$$\Delta^{\mathrm{T}}\mathcal{U} = -(\Delta^{\mathrm{T}}\mathbb{D}_y^{\mathrm{b}} - \mathbb{D}_y^{\mathrm{h}}\Delta^{\mathrm{T}})\Omega, \tag{A.15}$$

$$\Delta^{\mathrm{T}}\mathcal{V} = (\Delta^{\mathrm{T}}\mathbb{D}_x^{\mathrm{b}} - \mathbb{D}_x^{\mathrm{h}}\Delta^{\mathrm{T}})\Omega, \tag{A.16}$$

$$\Delta^{\mathrm{T}}\Omega = \dot{\Theta}, \tag{A.17}$$

where Θ is a column vector of hinge angles. We are interested in relating the velocity of every other body (denoted by $N_{\mathrm{h}} \times 1$ column vectors $\mathcal{U}'$, $\mathcal{V}'$ and Ω') in terms of the reference body velocity $\mathcal{U}_k = (U_k, V_k, \Omega_k)^{\mathrm{T}}$ and the hinge angular velocities $\dot{\Theta}$. The padded progressive sum matrix, $\widetilde{\mathbb{S}}(k)$, can be used for this purpose, via relation (A.9), to obtain

$$\mathcal{U}' = \mathbb{L}_U \mathcal{U}_k - \mathbb{H}_y(k)\dot{\Theta}, \tag{A.18}$$

$$\mathcal{V}' = \mathbb{L}_V \mathcal{U}_k + \mathbb{H}_x(k)\dot{\Theta}, \tag{A.19}$$

$$\Omega' = \mathbb{L}_\Omega \mathcal{U}_k + \mathbb{S}(k)\dot{\Theta}. \tag{A.20}$$

The matrices $\mathbb{L}_U$, $\mathbb{L}_V$ and $\mathbb{L}_\Omega$ are $N_h \times 3$, with row entries $(1, 0, -(Y_j - Y_k))$, $(0, 1, X_j - X_k)$, and $(0, 0, 1)$, respectively, for $j = 1, \ldots, N_b$ (with row k excluded). The $N_h \times N_h$ hinge influence matrix $\mathbb{H}_x(k)$ is defined as

$$\mathbb{H}_x(k) = \begin{pmatrix} X_1^h - X_1 & \cdots & X_{k-1}^h - X_1 & 0 & \cdots & 0 \\ 0 & \cdots & X_{k-1}^h - X_2 & 0 & \cdots & 0 \\ \vdots & & \vdots & \vdots & & \vdots \\ 0 & & X_{k-1}^h - X_{k-1} & 0 & \cdots & 0 \\ 0 & \cdots & 0 & X_{k+1} - X_k^h & \cdots & 0 \\ \vdots & & \vdots & \vdots & & \vdots \\ 0 & \cdots & 0 & X_{N_b-1} - X_k^h & \cdots & 0 \\ 0 & \cdots & 0 & X_{N_b} - X_k^h & \cdots & X_{N_b} - X_{N_h}^h \end{pmatrix} \tag{A.21}$$

and $\mathbb{H}_y(k)$ is identical, with X replaced by Y.

The relative accelerations can be found by differentiating (A.18),(A.19),(A.20) with respect to time, resulting in

$$\dot{\mathcal{U}}' = \mathbb{L}_U \dot{\mathcal{U}}_k - \mathbb{H}_y(k)\ddot{\Theta} + \mathcal{C}_U \tag{A.22}$$

$$\dot{\mathcal{V}}' = \mathbb{L}_V \dot{\mathcal{U}}_k + \mathbb{H}_x(k)\ddot{\Theta} + \mathcal{C}_V \tag{A.23}$$

$$\dot{\Omega}' = \mathbb{L}_\Omega \dot{\mathcal{U}}_k + \mathbb{S}(k)\ddot{\Theta}. \tag{A.24}$$

The entries in the $N_h \times 1$ centripetal acceleration vector, $\mathcal{C}_U$, are defined by

$$\mathcal{C}_{U,i} = \begin{cases} -\Omega_i^2(X_i - X_i^h) - \sum_{j=i+1}^{k-1} \Omega_j^2(X_{j-1}^h - X_j^h) - \Omega_k^2(X_{k-1}^h - X_k), \\ i = 1, \ldots, k-1 \\ -\Omega_k^2(X_k^h - X_k) - \sum_{j=k+1}^{i} \Omega_j^2(X_j^h - X_{j-1}^h) - \Omega_{i+1}^2(X_{i+1} - X_i^h), \\ i = k+1, \ldots, N_h \end{cases} \tag{A.25}$$

and $\mathcal{C}_V$ is identical, with X replaced by Y.

Now, the dynamics are specialized to the two problem classes of interest.

A.2. Problem 1: free swimming linked system

In this case, the system of linked bodies is subject only to the fluid dynamic forces; the hinge angles are prescribed functions of time. For these free swimming problems, Eqs. (A.3)–(A.5) can be summed over all bodies in the linked system to eliminate the constraint forces and moments, using the $1 \times N_b$ summation operator $\Sigma = (1, 1, \ldots, 1)$. Then, the constraint Eqs. (A.22)–(A.24) can be substituted for the non-reference body accelerations. After grouping terms together, the resulting system of three equations for the reference body velocity components can be written as

$$\mathbb{M}_k \dot{\mathcal{U}}_k = -\mathbb{M}_{\theta k} \ddot{\Theta} + \mathcal{F}_k^f + \mathcal{J}_k + \mathcal{G}_k, \tag{A.26}$$

where the 3×3 inertia matrix $\mathbb{M}_k$ is

$$\mathbb{M}_k = \sum_j \begin{pmatrix} m_j & 0 & -m_j(Y_j - Y_k) \\ 0 & m_j & m_j(X_j - X_k) \\ -m_j(Y_j - Y_k) & m_j(X_j - X_k) & (I_j + m_j|\boldsymbol{X}_j - \boldsymbol{X}_k|^2) \end{pmatrix} \qquad (A.27)$$

and the hinge input inertia matrix and the constraint forces are, respectively

$$\mathbb{M}_{\theta k} = \begin{pmatrix} -\Sigma'\mathbb{M}'\mathbb{H}_y(k) \\ \Sigma'\mathbb{M}'\mathbb{H}_x(k) \\ \Sigma'\mathbb{M}'(\mathbb{D}_x^{b'}\mathbb{H}_x(k) + \mathbb{D}_y^{b'}\mathbb{H}_y(k)) + \Sigma'\mathbb{I}'\mathbb{S}(k) \end{pmatrix}, \quad \mathcal{J}_k = \begin{pmatrix} -\Sigma'\mathbb{M}'\mathcal{C}_U \\ -\Sigma'\mathbb{M}'\mathcal{C}_V \\ -\Sigma'\mathbb{M}'(-\mathbb{D}_y^{b'}\mathcal{C}_U + \mathbb{D}_x^{b'}\mathcal{C}_V) \end{pmatrix}. \qquad (A.28)$$

Here, we use $()'$ to denote vectors and matrices in which the kth row and/or column has been excluded: $\mathbb{M}'$ and $\mathbb{I}'$ are the $N_h \times N_h$ diagonal matrices with masses and moments of inertia for non-reference bodies, and $\mathbb{D}_x^{b'}$ and $\mathbb{D}_y^{b'}$ are the same as their unprimed counterparts with kth row and column removed. The final terms in (A.26) represent, respectively, the sum of the forces and moments exerted by the fluid on all bodies in the linked system, and the net gravity/buoyancy force

$$\mathcal{F}_k^f = \begin{pmatrix} \Sigma\mathcal{F}_x^f \\ \Sigma\mathcal{F}_y^f \\ \Sigma(\mathcal{M}^f - \mathbb{D}_y^b\mathcal{F}_x^f + \mathbb{D}_x^b\mathcal{F}_y^f) \end{pmatrix}, \quad \mathcal{G}_k = \sum_j (\rho_j - \rho_f)A_j \begin{pmatrix} g_x \\ g_y \\ -(Y_j - Y_k)g_x + (X_j - X_k)g_y \end{pmatrix}. \qquad (A.29)$$

The three momentum equations are supplemented with the evolution equations for the position and angle of the reference body

$$\dot{\mathcal{X}}_k = \mathcal{U}_k. \qquad (A.30)$$

Once these equations are advanced, the constraint equations can be used to fill out the remaining body configurations.

A.3. Problem 2: Flexible multi-component wing

For this class of problems, we are interested in solving for the hinge deflection angles, θ_j, in response to prescribed motion of the reference body, $\mathcal{U}_k$. It is important to formulate the governing equations with the hinge moments preserved (for introducing stiffness and damping), but with the hinge forces removed. For this purpose, we substitute the relations (A.10) and (A.11) into the angular momentum equations. The equation for the kth body is ignored, and we find that

$$-\mathbb{D}_y^{bh'}\mathbb{M}'\dot{\mathcal{U}}' + \mathbb{D}_x^{bh'}\mathbb{M}'\dot{\mathcal{V}}' + \mathbb{I}'\dot{\Omega}' = \mathcal{M}^{f'} - \mathbb{D}_y^{bh'}\mathcal{F}_x^{f'} + \mathbb{D}_x^{bh'}\mathcal{F}_y^{f'} + \Delta'\mathcal{M}^h + (\mathbb{M}' - \mathbb{M}_f')(-\mathbb{D}_y^{bh'}\mathcal{G}_x' + \mathbb{D}_x^{bh'}\mathcal{G}_y'), \qquad (A.31)$$

where Δ' is the differencing matrix, Δ, with the kth row removed, and $\mathbb{D}_x^{bh'}$ is the $N_h \times N_h$ matrix that truncates the kth row and column of the $N_b \times N_b$ matrix $\mathbb{D}_x^b - \Delta\mathbb{D}_x^h\widetilde{\mathbb{S}}^T(k)$. It can be shown that $\mathbb{D}_x^{bh'} = \Delta'\mathbb{H}_x^T(k)$ and $\mathbb{D}_y^{bh'} = \Delta'\mathbb{H}_y^T(k)$.

In this work, we assume a linear, damped Hookean model for the hinges, so $M_j^h = -K_j\theta_j - R_j\dot{\theta}_j$, or

$$\mathcal{M}^h = -\mathbb{K}\Theta - \mathbb{R}\dot{\Theta}, \qquad (A.32)$$

where $\mathbb{K}$ and $\mathbb{R}$ are $N_h \times N_h$ diagonal matrices with entries of torsion spring stiffnesses and hinge damping coefficients, respectively. When the constraints are substituted for the body velocity vectors in (A.31), and we multiply each term by the progressive summation operator $\mathbb{S}^T(k)$ to invert Δ', we arrive at the system of N_h equations

$$\mathbb{M}_\theta\ddot{\Theta} = -\mathbb{M}_{k\theta}\dot{\mathcal{U}}_k + \mathcal{F}_\theta^f + \mathcal{J}_\theta + \mathcal{G}_\theta - \mathbb{K}\Theta - \mathbb{R}\dot{\Theta}, \qquad (A.33)$$

where

$$\mathbb{M}_\theta = \mathbb{H}_x^{\mathsf{T}}(k)\mathbb{M}'\mathbb{H}_x(k) + \mathbb{H}_y^{\mathsf{T}}(k)\mathbb{M}'\mathbb{H}_y(k) + \mathbb{S}^{\mathsf{T}}(k)\mathbb{I}'\mathbb{S}(k), \tag{A.34}$$

$$\mathbb{M}_{k\theta} = -\mathbb{H}_y^{\mathsf{T}}(k)\mathbb{M}'\mathbb{L}_U + \mathbb{H}_x^{\mathsf{T}}(k)\mathbb{M}'\mathbb{L}_V + \mathbb{S}^{\mathsf{T}}(k)\mathbb{I}'\mathbb{L}_\Omega, \tag{A.35}$$

$$\mathcal{J}_\theta = \mathbb{H}_y^{\mathsf{T}}(k)\mathbb{M}'\mathcal{C}_U - \mathbb{H}_x^{\mathsf{T}}(k)\mathbb{M}'\mathcal{C}_V, \tag{A.36}$$

$$\mathcal{F}_\theta^{\mathrm{f}} = \mathbb{S}^{\mathsf{T}}(k)\mathcal{M}^{f'} - \mathbb{H}_y^{\mathsf{T}}(k)\mathcal{F}_x^{f'} + \mathbb{H}_x^{\mathsf{T}}(k)\mathcal{F}_y^{f'}, \tag{A.37}$$

$$\mathcal{G}_\theta = -\mathbb{H}_y^{\mathsf{T}}(k)(\mathbb{M}' - \mathbb{M}_{\mathrm{f}}')\mathcal{G}_x' + \mathbb{H}_x^{\mathsf{T}}(k)(\mathbb{M}' - \mathbb{M}_{\mathrm{f}}')\mathcal{G}_y'. \tag{A.38}$$

Eq. (A.33), split into a system of $2N_{\mathrm{h}}$ first-order equations, are to be solved for the hinge angles, Θ, for a given input vector, $\dot{\mathcal{U}}_k$. Once this equation is advanced, the remaining body positions and velocities can be set by applying the linkage constraints.

References

[1] D. Calhoun, A cartesian grid method for solving the two-dimensional streamfunction–vorticity equations in irregular regions, J. Comput. Phys. 176 (2002) 231–275.

[2] J.P. Christiansen, Numerical solution of hydrodynamics by the method of point vortices, J. Comput. Phys. 13 (1973) 363–379.

[3] G.-H. Cottet, P. Koumoutsakos, Vortex Methods: Theory and Practice, Cambridge University Press, 2000.

[4] G.-H. Cottet, P. Poncet, Advances in direct numerical simulations of 3D wall-bounded flows by vortex-in-cell methods, J. Comput. Phys. 193 (2003) 136–158.

[5] J.D. Eldredge, Numerical simulations of undulatory swimming at moderate Reynolds number, Bioinspir. Biomim. 1 (2006) S19–S24.

[6] J.D. Eldredge, Numerical simulation of the fluid dynamics of 2D rigid body motion with the vortex particle method, J. Comput. Phys. 221 (2) (2007) 626–648.

[7] C. Farhat, M. Lesoinne, N. Maman, Mixed explicit/implicit time integration of coupled aeroelastic problems: three-field formulation, geometric conservation and distributed solution, Int. J. Numer. Meth. Fluids 21 (1995) 807–835.

[8] R.D. Henderson, Details of the drag curve near the onset of vortex shedding, Phys. Fluids. 7 (9) (1995) 2102–2104.

[9] K.O.L.F. Jayaweera, B.J. Mason, The behaviour of freely falling cylinders and cones in a viscous fluid, J. Fluid Mech. 22 (4) (1965) 709–720.

[10] R. Kamakoti, W. Shyy, Fluid-structure interaction for aeroelastic applications, Prog. Aerosp. Sci. 40 (2004) 535–558.

[11] E. Kanso, J.E. Marsden, C.W. Rowley, J. Melli-Huber, Locomotion of articulated bodies in a perfect fluid, J. Nonlinear Sci. 15 (4) (2005) 255–289.

[12] P. Koumoutsakos, A. Leonard, F. Pépin, Boundary conditions for viscous vortex methods, J. Comput. Phys. 113 (1994) 52–61.

[13] Y. Lian, W. Shyy, D. Viieru, B. Zhang, Membrane wing aerodynamics for micro air vehicles, Prog. Aerosp. Sci. 39 (2003) 425–465.

[14] M.J. Lighthill, Introduction: boundary layer theory, in: L. Rosenhead (Ed.), Laminar Boundary Layers, Clarendon Press, 1961.

[15] M.J. Lighthill, Hydrodynamics of aquatic animal propulsion, Ann. Rev. Fluid Mech. 1 (1969) 413–446.

[16] P. Ploumhans, G.S. Winckelmans, Vortex methods for high-resolution simulations of viscous flow past bluff bodies of general geometry, J. Comput. Phys. 165 (2000) 354–406.

[17] D. Russell, Z.J. Wang, A cartesian grid method for modeling multiple moving objects in 2D incompressible viscous flow, J. Comput. Phys. 191 (2003) 177–205.

[18] D. Shiels, A. Leonard, A. Roshko, Flow-induced vibration of a circular cylinder at limiting structural parameters, J. Fluid Struct. 15 (2001) 3–21.

[19] K. Taira, T. Colonius, The immersed boundary method: a projection approach, J. Comput. Phys. 225 (2) (2007) 2118–2137.

[20] J. Toomey and J.D. Eldredge, Numerical and experimental investigation of the role of flexibility in flapping wing flight, AIAA Paper 2006-3211, 2006.

[21] J. Toomey and J.D. Eldredge, Numerical and experimental study of the fluid dynamics of a flapping wing with low order flexibility, Phys. Fluids in review.

[22] J.C. Wu, Theory of aerodynamic force and moment in viscous flows, AIAA J. 195 (4) (1981) 432–441.